https://doi.org/10.5194/egusphere-2026-3095
Preprint. Discussion started: 12 June 2026


# Temporal variability of measured vertical velocity over a canyon-incised slope in the Coral Sea

Kévin Robache[1], Anne A. Petrenko[1], Mathieu Gentil[1,2], Louise Rousselet[2], and Sophie Bonnet[1]

[1]Mediterranean Institute of Oceanography (MIO), Aix-Marseille Université, Université de Toulon, CNRS, IRD, 13288 Marseille CEDEX 09, France
[2]Laboratoire d'Études en Géophysique et Océanographie Spatiales (LEGOS), Université de Toulouse, CNES, CNRS, IRD, 31400 Toulouse, France

**Correspondence:** Kévin Robache (kevin.robache@univ-amu.fr)

**Abstract.** Oceanic vertical velocity ($w$) is often neglected due to its small magnitude compared to horizontal currents. However, it plays a fundamental role in coupling the ocean surface with its interior, with major implications for a wide range of physical and biogeochemical processes. In this study, four ADCPs were deployed on fixed Eulerian moorings and collected $w$ measurements over slightly less than one year, covering the water column from 50 to 410 m depth. Using a combined approach based on Fourier spectral analysis and Ensemble Empirical Mode Decomposition, the variance distribution was characterized. The spectral analysis highlights the fundamental anisotropy of the flow, as vertical and horizontal velocities exhibit distinctly different spectral properties. While horizontal currents are mainly constrained by topography, vertical motions are primarily driven by internal gravity waves and intermittent small-scale processes. Furthermore, a persistent $w$ signal at synoptic scales shows that the velocity is not purely geostrophic at all temporal scales. The results show that the variability of $w$ time series is primarily dominated by short timescales, on the order of a few days or less. The data are also strongly influenced by biologically driven diel vertical migrations, which impose a pronounced periodic signal. The overall dynamics of the study area, strongly influenced by a canyon-incised slope topography, is characterized by a prevailing weak downwelling regime (3–4 mm $s^{-1}$), intermittently disrupted by short-lived (few days) strong upwelling events (exceeding the 90$^{th}$ percentile of 1-day moving averaged $w$ data). Finally, our results suggest that the canyons could act as an efficient tracer sink (e.g., carbon), with vertical velocities reaching several mm $s^{-1}$.

## 1 Introduction

Ocean dynamics are inherently non-linear and span a wide range of spatial and temporal scales, making them particularly challenging to fully characterize. Within this complex three-dimensional system, vertical velocity (denoted $w$) plays a fundamental role. Although often neglected in studies of ocean circulation because its magnitude (mm $s^{-1}$) is several orders smaller than that of horizontal currents (cm $s^{-1}$ to m $s^{-1}$), vertical motion constitutes a key mechanism linking the ocean surface to its interior. This vertical connectivity has major implications across multiple spatial and temporal scales, particularly in biogeochemical processes: vertical velocities can directly influence phytoplankton distribution (Denman and Gargett, 1983; Strass, 1992; Rodríguez et al., 2001; Rousselet et al., 2019; Tzortzis et al., 2021; Fuchs et al., 2023), regulate nutrient transport and

https://doi.org/10.5194/egusphere-2026-3095
Preprint. Discussion started: 12 June 2026


diffusion (Lilover et al., 2003; Barceló-Llull et al., 2016; Freilich and Mahadevan, 2019), and modulate carbon cycling and export (Dall'Olmo et al., 2016; Nowicki et al., 2022; Siegel et al., 2023; Burd, 2024).

Despite its importance, the multiscale dynamics of the vertical component $w$ remains poorly understood. This knowledge gap stems in part from the intrinsic difficulty of measuring vertical velocities in the ocean (Liang et al., 2017; Comby et al., 2022; Zhu et al., 2023; Carli et al., 2024; He and Mahadevan, 2024; Arnaud et al., 2025). For a long time, direct observations of $w$ were considered nearly impossible because of their weak amplitude relative to instrumental noise and platform motion. As a result, vertical velocities have often been inferred indirectly from dynamical balances (e.g., geostrophic theory, quasi-geostrophic omega equation, horizontal divergence/convergence through mass continuity) or derived from numerical models, rather than measured *in situ*. However, indirect estimates are generally limited by underlying assumptions and may fail to capture the full spectrum of variability, particularly at submesoscale and smaller scales where ageostrophic processes become significant. Although Acoustic Doppler Current Profilers (ADCPs) have long been used to measure ocean currents, recent advances in extracting the faint vertical velocity signal from high-resolution mooring data now provide new opportunities to directly observe $w$ over extended periods (e.g., D'Asaro et al., 1996; D'Asaro, 2001; Thurnherr, 2011; Thurnherr et al., 2015; Houpert et al., 2016; D'Asaro et al., 2018; Comby et al., 2022; Arnaud et al., 2025). Such observations open the door to a more comprehensive characterization of $w$ variability across scales, from high-frequency fluctuations to longer-term modulations. Yet, a detailed multiscale description of *in situ* vertical velocity time series remains scarce, especially in oligotrophic oceanic regions where biogeochemical sensitivity to vertical exchanges is particularly high. In such nutrient-limited environments, vertical exchanges represent a primary mechanism by which subsurface nutrient reservoirs can influence surface biological activity (Lewis et al., 1986; Calil and Richards, 2010; Pan et al., 2012; Landou et al., 2023; Ma et al., 2023). Even moderate vertical motions, if organized over specific temporal scales, may therefore have significant ecological consequences. Characterizing the temporal structure of $w$ variability is thus essential to better constrain its potential role in regulating biogeochemical fluxes. Addressing this gap is therefore key to improving our understanding of the physical–biogeochemical coupling that governs ecosystem functioning and carbon export in these environments.

Despite the growing availability of long-term moored observations, fundamental questions remain regarding the temporal organization of vertical velocity variability. In particular, it is still unclear which temporal scales dominate the observed signal, how robust these dominant frequencies are over time, and to what extent different dynamical regimes can be distinguished within a single time series. Most existing studies either focus on specific frequency bands or rely on model-based diagnostics, leaving a gap in the comprehensive characterization of *in situ* vertical velocity records across the full accessible spectrum of variability. Addressing these questions is essential for placing local observations within a broader dynamical framework and for better constraining the physical drivers of vertical exchanges. The objective of this study is to conduct a multiscale analysis of several $w$ time series recorded in the Western Subtropical South Pacific Ocean, in order to characterize their variability across a broad range of temporal scales, identify dominant frequency bands, and examine their temporal modulation using complementary spectral and time–frequency approaches.

The study area, data acquisition methods, and statistical analyzes are described in Section 2. The results are presented in Section 3. We first provide a data presentation in Section 3.1, then examine the multiscale variability of vertical velocity in

https://doi.org/10.5194/egusphere-2026-3095
Preprint. Discussion started: 12 June 2026


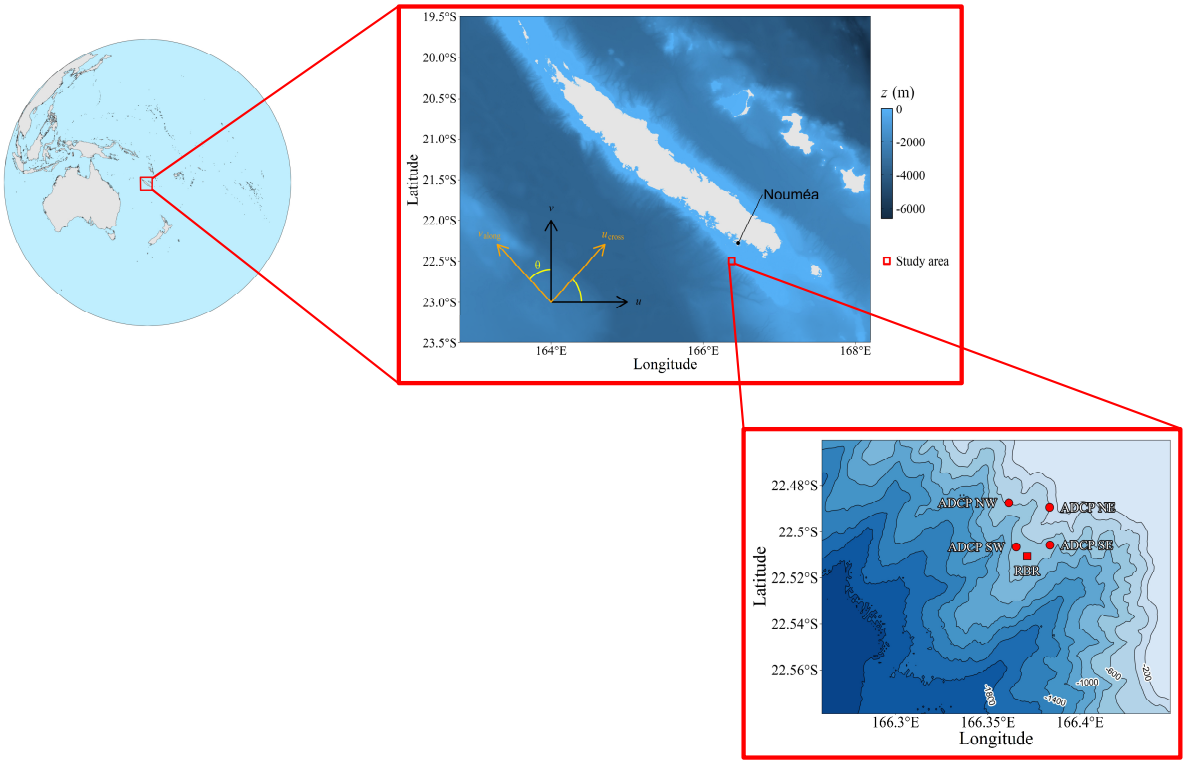


**Figure 1.** Map of the study area located in the Coral Sea (Western Subtropical South Pacific) off Nouméa (Grande Terre island, New Caledonia, France). The location of the four ADCPs and of the RBR© sensors is shown.

Section 3.2, and next focus on selected specific events in Section 3.3. Finally, the results are discussed in Section 4, and the main conclusions are summarized in Section 5.

## 2 Materials and methods

### 2.1 ADCPs measurements

#### 2.1.1 Vertical velocity

Four Teledyne Marine© RD Instruments (RDI) 75 kHz 4 Beams ADCPs were deployed on four fixed moorings from 4 March 2024 to 22 February 2025 off Nouméa (New Caledonia, France) in the Coral Sea (Western Subtropical South Pacific Ocean). A map of the study area is shown in Figure 1. This region was selected because of its intense atmospheric dinitrogen ($N_2$) fixation activity, among the highest observed in the global ocean (Bonnet et al., 2017; Shao et al., 2023). Through this process, small organisms such as *Trichodesmium* spp. enriches the surrounding oligotrophic waters with bioavailable nitrogen,

https://doi.org/10.5194/egusphere-2026-3095
Preprint. Discussion started: 12 June 2026


thereby supporting the growth of other phytoplankton and enhancing primary production (Berthelot et al., 2016; Bonnet et al., 2016; Benavides et al., 2017, 2022; Bonnet et al., 2026). Nitrogen fixation in this region is therefore closely linked to key biogeochemical processes, particularly the stimulation of carbon sequestration and enhanced particulate carbon export to the deep ocean (Savarino et al., 2025; Bonnet et al., 2026). It is within this framework that the European Research Council HOPE project (principal investigator Sophie Bonnet) was established, aiming to investigate the role of diazotrophy in oceanic biogeochemical cycles. The present study is part of the AMidex HOPE-VV project (principal investigator Anne A. Petrenko), which constitutes the physical oceanography component of HOPE and focuses specifically on characterizing vertical velocity variability and its implications for physical–biogeochemical coupling.

Water depth varies substantially across the study area, ranging from 396 m at Site NE, the most coastal location, to 762 m at Site SW, the most offshore site. Sites NW and SE lies at intermediate depths of 635 m and 687 m, respectively (see Figure 1). The ADCPs were deployed at depth, upward-looking, with the instrument head positioned at 450 m (except for site NE, due to shallower bathymetry). This configuration provides velocity time series covering depths from 50 to 410 m, with an approximate vertical resolution of 20 m. In our case, the time resolution of the ADCPs was 2 hours, yielding time series of 4,272 observations at each depth with a missing value ratio ranging between 1 % and 2 %.

Each of these ADCPs was composed of four acoustic beams that measure the Doppler shift of sound scattered by particles in the water column to derive velocity profiles. To obtain reliable estimates of the vertical velocity component $w$, the ADCPs measure velocities over 2-minute intervals and retain the averaged value. We followed the processing approach described by Comby et al. (2022). This method includes strict quality criteria on the returned signal and the projection of along-beam velocities into the Earth reference frame, with corrections for instrument orientation (pitch, roll, and heading). These processing steps are critical because the amplitude of $w$ in open-ocean conditions is on the order of $10^{-3}$ m s$^{-1}$, making it particularly sensitive to measurement noise and mooring motion without careful treatment (Comby et al., 2022).

### 2.1.2 Cartesian rotation

Processed in the Earth reference frame, the ADCP data also yielded zonal ($u$) and meridional ($v$) velocities. To align these velocity components with the south-western coast of New Caledonia, we applied a Cartesian coordinate rotation. Following the coastal orientation described by Ganachaud et al. (2010), the coordinate system was rotated such that the positive along-shore axis points northwestward (geographic heading of 315°). The resulting cross-shore (positive offshore) and along-shore (positive northwestward) velocities were computed as follows:

$$\begin{pmatrix} u_{\text{cross}} \\ v_{\text{along}} \end{pmatrix} = \begin{pmatrix} \cos\theta & \sin\theta \\ -\sin\theta & \cos\theta \end{pmatrix} \begin{pmatrix} u \\ v \end{pmatrix} \tag{1}$$

where $\theta = \pi/4$ radians ($= 45°$) represents the corresponding trigonometric rotation angle applied to the standard East-North reference frame, and $u_{\text{cross}}$ and $v_{\text{along}}$ represent the rotated cross-shore (perpendicular to the coast) and along-shore (parallel to the coast) velocity components, respectively. This rotation is illustrated in Figure 1 by the orange axes, which are rotated relative to the standard geographic reference frame (black axes). As an example, the typical southeastward-flowing current in

https://doi.org/10.5194/egusphere-2026-3095
Preprint. Discussion started: 12 June 2026


this region, known as the Alis Current of New Caledonia (ACNC; Ganachaud et al., 2010; Marchesiello et al., 2010; Cravatte et al., 2015), is therefore characterized by $v_{\mathrm{along}} < 0$ m s$^{-1}$ (flowing southeastward along the coast).

### 2.2 Statistical analyses

#### 2.2.1 Fourier spectral analysis

Vertical velocity time series are often characterized by a superposition of signals associated with different dynamical regimes, whose relative contributions may vary over time. Internal waves, mesoscale variability, and lower-frequency modulations can coexist within the same record (Garrett, 1979; Garrett and Munk, 1979; Skyllingstad et al., 1996; Wunsch and Ferrari, 2004; Taylor and Thompson, 2023), making their identification non-trivial. A rigorous multiscale analysis is therefore required to disentangle the dominant temporal components and to assess how energy is distributed across frequencies. For this purpose, we used Fourier spectral analysis. The analyzed time series contain data gaps due to technical failures (1–2 %). To estimate the Fourier spectral density despite these discontinuities, we applied the Wiener–Khinchin theorem (Wiener, 1930; Khintchine, 1934). Under the assumption of weak stationarity, this theorem states that the power spectral density is given by the Fourier transform of the autocorrelation function. The autocorrelation is defined as:

$$C(\tau) = \left\langle \bar{X}(t)\bar{X}(t+\tau) \right\rangle, \tag{2}$$

where $\langle\cdot\rangle$ denotes the statistical average, and $\bar{X}(t)$ denotes the standardized time series $X(t)$, normalized to zero mean and unit variance prior to the analysis. The resulting autocorrelation function is then Fourier-transformed (using the fast Fourier transform, FFT) to obtain the spectral density:

$$E(f) = \int_{-\infty}^{+\infty} C(\tau) e^{-i2\pi f\tau}\, \mathrm{d}\tau, \tag{3}$$

where $f$ is the frequency and $E(f)$ denotes the power spectral density. Under this normalization, the total variance of the time series is conserved in the spectral domain according to the Parseval-Plancherel theorem (variance-preserving decomposition; Parseval des Chênes, 1806; Plancherel, 1910). Mathematically, this implies that the integral of the spectral density equals the variance of the time series:

$$\int_{-\infty}^{+\infty} E(f)\, \mathrm{d}f = \left\langle |\bar{X}(t)|^2 \right\rangle \tag{4}$$

For a standardized stationary process, this yields:

$$\int_{-\infty}^{+\infty} E(f)\, \mathrm{d}f = C(0) = 1, \tag{5}$$

since the autocorrelation at zero lag equals the variance. Due to this property, the normalized spectral density can be rescaled by the original variance ($\sigma^2$) of the time series $X(t)$ to obtain the absolute variance associated with each specific scale:

$$S(f) = E(f)\sigma^2 \tag{6}$$

https://doi.org/10.5194/egusphere-2026-3095
Preprint. Discussion started: 12 June 2026


For these spectra, a power-law behavior is classically expected (Schmitt and Huang, 2016) such that:

$$E(f) \sim f^{-\beta}, \tag{7}$$

where "$\sim$" denotes proportionality. For example, the value $\beta = 5/3$ is expected for velocities in the framework of homogeneous and isotropic 3D turbulence (Kolmogorov, 1941; Obukhov, 1941).

### 2.2.2 Ensemble empirical mode decomposition

Classical Fourier spectral analysis provides a robust and widely used framework to characterize the global frequency content of a time series and to identify its dominant periodicities. To further examine how variance is distributed across characteristic temporal scales, we complement this global description with Ensemble Empirical Mode Decomposition (EEMD; Wu and Huang, 2009). EEMD extends Empirical Mode Decomposition (EMD; Huang et al., 1998), a fully data-adaptive method that decomposes a signal into intrinsic mode functions (IMFs), representing oscillatory components directly extracted from the data without imposing a priori basis functions. EEMD enhances the robustness of this decomposition by adding white-noise realizations to the signal and averaging over an ensemble, thereby mitigating mode mixing and stabilizing the identification of physically meaningful scales. EEMD decomposes the time series $X(t)$ into a finite set of nearly zero-mean intrinsic mode functions $C_i(t)$ and a residual term $r_n(t)$:

$$X(t) = \sum_{i=1}^{n} C_i(t) + r_n(t), \tag{8}$$

where $r_n(t)$ represents the low-frequency residue, typically associated with the trend of the time series. These IMFs isolate oscillatory modes with locally defined amplitude and frequency content.

The spectral properties of each mode are then characterized using Fourier analysis in order to estimate a representative mean temporal scale (Huang et al., 1998, 2009):

$$\overline{t_i} = \left( \frac{\int_0^\infty f S_i(f) \mathrm{d}f}{\int_0^\infty S_i(f) \mathrm{d}f} \right)^{-1}, \tag{9}$$

where $S_i(f)$ is the Fourier spectral density of $C_i(t)$. This combined EEMD–Fourier framework enables (i) the identification of intrinsic oscillatory modes, (ii) the attribution of each mode to a characteristic mean timescale, and (iii) the quantification of the variance associated with each scale component ($\sigma_i{}^2 = \sigma(C_i)^2$). The approach thus provides a scale-resolved description of variance distribution while remaining fully consistent with the global Fourier spectrum of the original signal.

### 2.2.3 Cross-correlation function

Cross-correlation analyses were performed between the IMFs of different time series in order to investigate their relationships at different time scales. For two time series $X(t)$ and $Y(t)$ with zero mean and unit standard deviation, the cross-correlation function is defined as:

$$\rho_{X,Y}(\tau) = \langle X(t) Y(t+\tau) \rangle \tag{10}$$

https://doi.org/10.5194/egusphere-2026-3095
Preprint. Discussion started: 12 June 2026


The cross-correlation function quantifies the statistical similarity between the two time series as a function of the time lag $\tau$. Positive values of $\rho_{X,Y}(\tau)$ indicate that the two signals tend to vary in the same direction, whereas negative values indicate an opposite behavior.

#### 2.2.4 Probability density functions quotient

To further characterize the statistical dependence between time series, we analyze the quotient of their probability density functions (PDFs). Probability density functions provide a compact description of the distribution of a time series. The PDF quotient between two time series $X(t)$ and $Y(t)$ in the $(x,y)$ plane is defined as (Xu et al., 2007):

$$Q(x,y) = \log_{10}\left(\frac{P_{X,Y}(x,y)}{P_X(x)P_Y(y)}\right), \tag{11}$$

where $P_{X,Y}(x,y)$ is the joint PDF of $X(t)$ and $Y(t)$, and $P_X(x)$ and $P_Y(y)$ are their respective marginal PDFs. Under statistical independence, $P_{X,Y}(x,y) = P_X(x)P_Y(y)$, and therefore $Q(x,y) = 0$. Positive values of $Q$ indicate combinations of amplitudes that occur more frequently than expected under independence (a "positive" dependence), while negative values indicate combinations that are less likely than expected (a "negative" dependence). This method has for example been used in oceanography to analyze environmental time series relationships (Robache and Schmitt, 2025a, 2026b, a).

#### 2.2.5 Moving average

A moving average was applied to smooth the time series and highlight the underlying variability. For a time series $X(t)$, the moving average $\tilde{X}(t)$ is defined as

$$\tilde{X}(t) = \frac{1}{N}\sum_{k=-m}^{m} X(t+k), \tag{12}$$

where $N$ is the window length and $m = (N-1)/2$. This procedure reduces high-frequency variability while preserving longer-term trends in the data. It therefore acts as a low-pass filter.

## 3 Results

### 3.1 Data presentation

#### 3.1.1 Diel vertical migrations

It is well known that biological vertical motions can affect the $w$ values estimated by the ADCP (Schott and Johns, 1987; Flagg and Smith, 1989; Ott, 2005; van Haren, 2007; van Haren and Compton, 2013), thereby preventing the observation of purely "physical" variability. This bias, particularly linked to diel vertical migrations (DVMs), is periodic and follows the solar cycle (Forward, 1976; Hays, 2003). Visually, it is evident that this bias is present in our data. An example is shown in panel (a) of Figure 2. The DVMs are clearly visible as high positive (at sunset) and negative (at sunrise) vertical velocities (on the order of cm $s^{-1}$) that are periodic and coherent with depth.

https://doi.org/10.5194/egusphere-2026-3095
Preprint. Discussion started: 12 June 2026


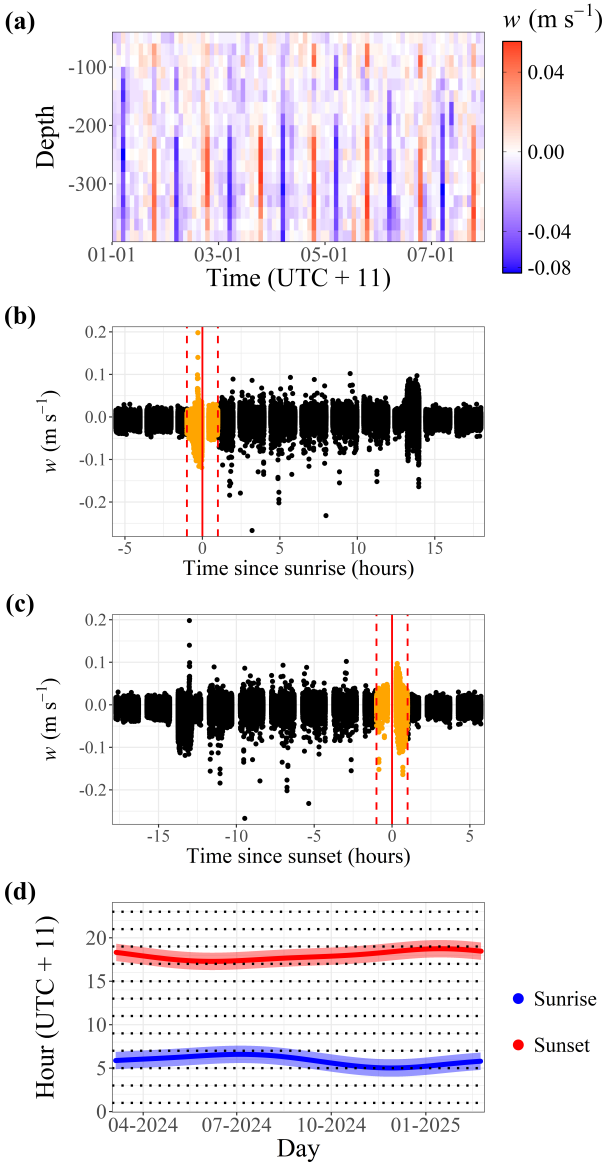


**Figure 2.** Diel vertical migration signal in ADCP-derived vertical velocities. **(a)** Time–depth distribution of vertical velocity $w$ from 1 to 8 January 2025 (SW site). **(b, c)** Vertical velocity relative to local sunrise **(b)** and sunset **(c)**; orange points and red dashed lines indicate data within $\pm 1$ h of the solar transitions used to identify first-order DVMs. **(d)** Seasonal evolution of local sunrise and sunset times ($\pm 1$ h range indicated by the shaded area), illustrating how variations in sampling time (dashed lines) relative to these transitions lead to differences in the observed DVM amplitude.

To try to isolate these DVMs, we used local sunset and sunrise times from the SunEarthTool website (https://www.sunearthtools.com/, last access: 26 January 2026). By comparing the sampling time with these times, we obtained the results presented in

https://doi.org/10.5194/egusphere-2026-3095
Preprint. Discussion started: 12 June 2026


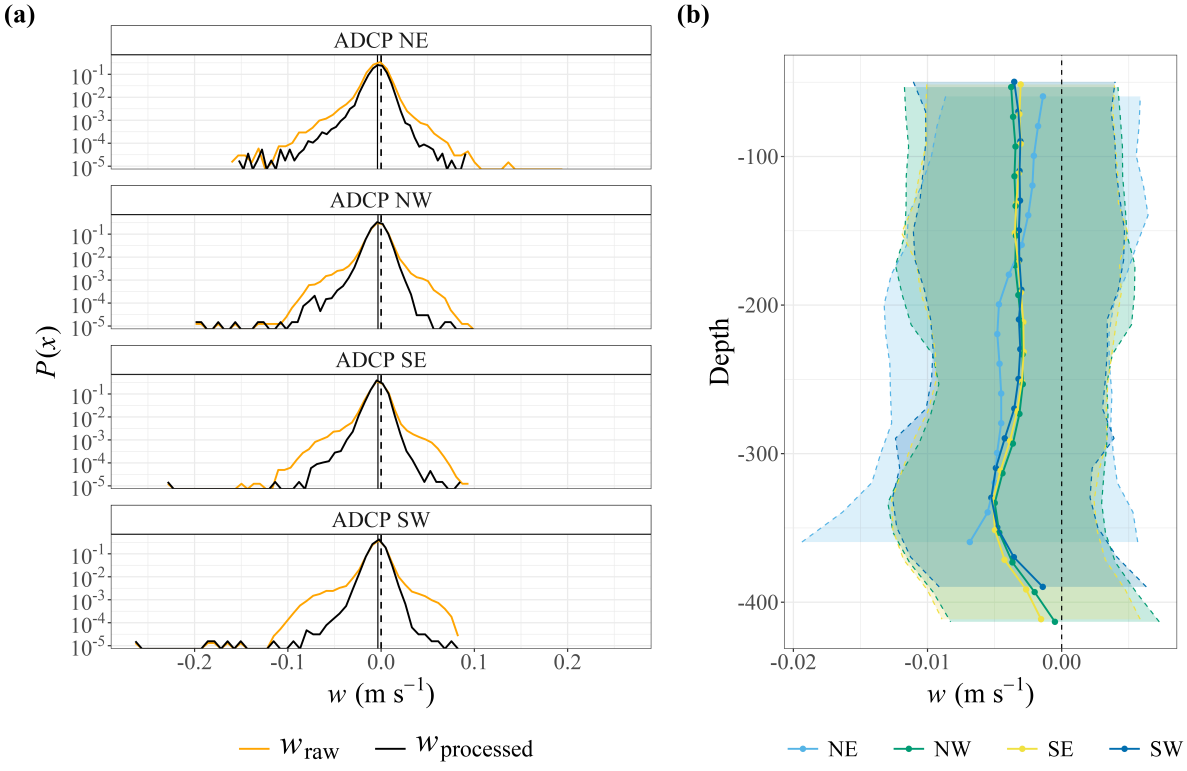


**Figure 3. (a)** Probability density functions (PDFs) of the vertical velocity $w$ with ($w_{\mathrm{raw}}$) and without ($w_{\mathrm{processed}}$) first-order DVMs, and **(b)** vertical profiles of the mean (lines) and standard deviation (shaded areas) of $w_{\mathrm{processed}}$ for the NE, NW, and SE sites. Black dashed lines in (a, b) indicate $w = 0$, and the solid black line in (a) represents the site mean $w_{\mathrm{processed}}$ value. The bandwidths used to calculate the PDFs are equal to 2 % of the difference between the maximum and the minimum value of the considered data set. The value represented on the $x$ axis is the middle value of each range. In (a), the stations are classified from top to bottom corresponding to increasing location depths.

panels (b), (c), and (d) of Figure 2. First, a one-hour window was chosen empirically after sensitivity tests before and after sunrise and sunset to select the data most affected by the DVMs. These data are shown as colored points in panels (b) and (c). For the remainder of the study, we refer to $w_{\mathrm{raw}}$ ($w_{\mathrm{processed}}$) the velocity data including (respectively filtering) these "first-order DVMs". Second, the amplitude of the captured DVMs is not constant throughout the year. This can be due to biological variability but is is also due to the times at which sunrise and sunset occur relative to the sampling times (every two hours). This is illustrated in panel (d). Studying for example the case of sunrise, sampling always occurs at 5:00 h and 7:00 h (local time). The closer sunrise occurs to 5:00 h or 7:00 h, the stronger the DVM is detected. But if sunrise occurs just in between (around 6:00 h), it can go relatively undetected as in late March 2024 and early September 2024. Similarly, sunset occuring around 17:00 h, between the ADCP sampling times of 16:00 h and 18:00 h, can go undetected late March and mid-October

https://doi.org/10.5194/egusphere-2026-3095
Preprint. Discussion started: 12 June 2026


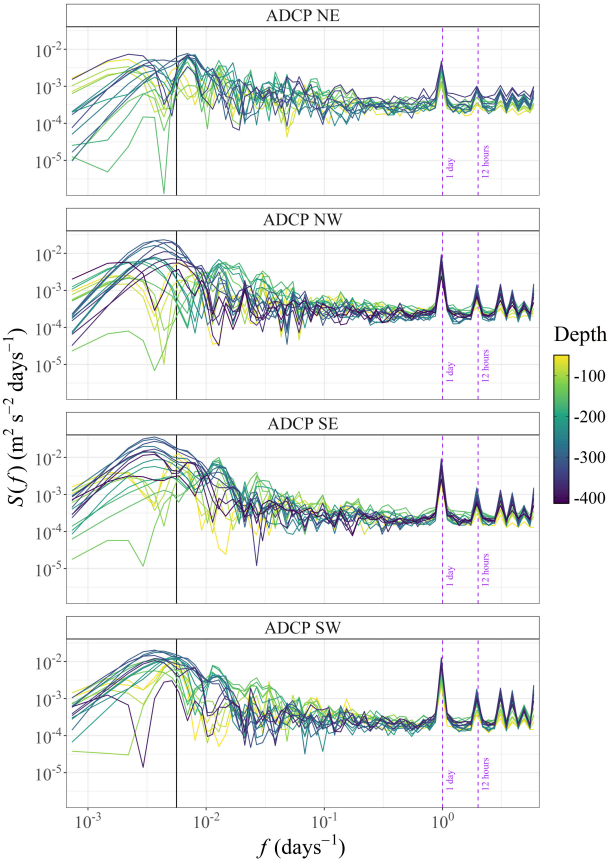


**Figure 4.** Fourier spectral density $S(f) = E(f)\sigma^2$ of $w_{\mathrm{raw}}$ time series for each site. The spectra were smoothed using a mean per decade. The vertical black line indicates the Shannon-Nyquist frequency (i.e., the highest frequency resolved with at least two samples per period).

2024. For these periods, the measurements are therefore further from the core of the first-order DVM, and a weaker influence of these migrations on the data can be expected.

### 3.1.2 Distributions and mean profiles

Figure 3 shows the distribution of $w_{\mathrm{raw}}$ and $w_{\mathrm{processed}}$ data (panel a) as well as the means and standard deviations ($w_{\mathrm{processed}}$; panel b) as a function of depth for each site.

First, considering the distributions (panel a), an asymmetry is observed for each PDF, with larger values on the negative side than on the positive side. This feature is even more pronounced for the PDFs where the values associated with first-order DVMs have been removed (black curves). These curves also allow us to identify the sites where the impact of DVMs is the strongest in the $w$ data. Indeed, the NW, SW, and SE sites appear to be more affected when comparing the distributions with and without these first-order DVMs. The distributions are generally similar across the NW, SW, and SE sites. In contrast, the

https://doi.org/10.5194/egusphere-2026-3095
Preprint. Discussion started: 12 June 2026


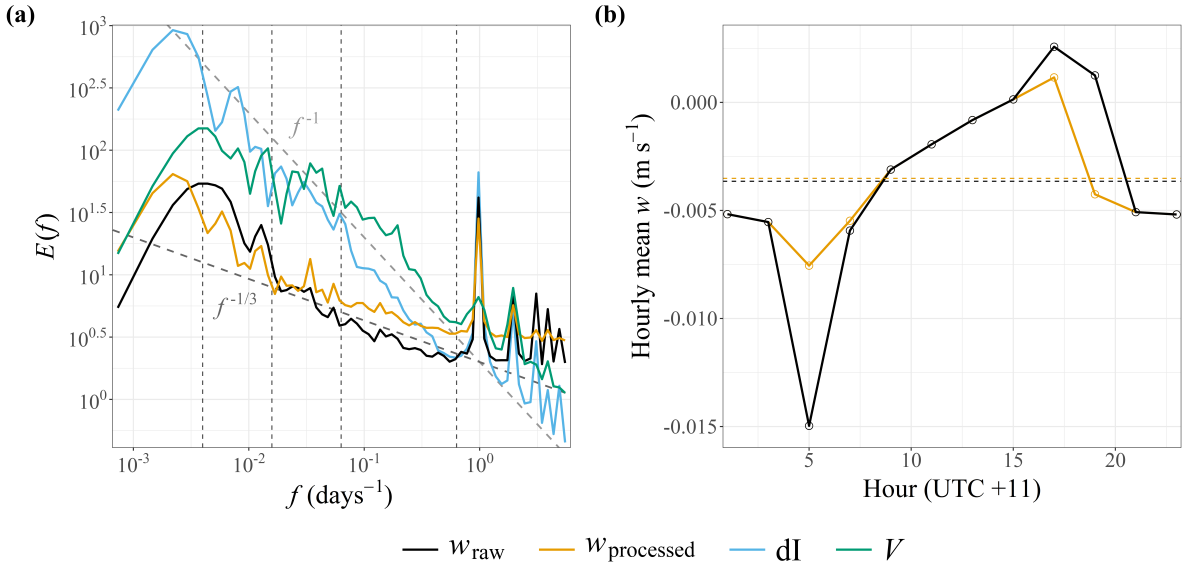


**Figure 5.** **(a)** Fourier spectral density $E(f)$ for the $w$ time series with ($w_{\text{raw}}$) and without ($w_{\text{processed}}$) first-order DVMs, as well as for the dI and $V$ time series. The $\beta = 1$ and $\beta = 1/3$ power laws are shown by gray dashed lines. The vertical black dashed lines represent the boundaries used to estimate the scaling. **(b)** Hourly means of $w_{\text{raw}}$ and $w_{\text{processed}}$. The horizontal dashed lines indicate the mean values.

NE site, which is closest to the coast, exhibits a more pronounced negative tail in its distribution compared to the other sites. Finally, the overall means for each site are also indicated in the same panel (for $w_{\text{processed}}$). One can note that the mean values are negative for all sites. They are larger and more variable at the coastal site NE ($-0.004 \pm 0.009$ m s$^{-1}$), and similar for the SW and SE sites ($-0.003 \pm 0.007$ m s$^{-1}$). The NW site shows a mean similar to the last two sites, but exhibits slightly greater variability ($-0.003 \pm 0.008$ m s$^{-1}$). Although variability exceeds the mean in magnitude at all sites, the consistently negative values indicate a persistent background downward motion. This suggests that vertical transport results from the combination of a weak mean downwelling and strong intermittent fluctuations. The proportions of values above and below $w = 0$ m s$^{-1}$ were calculated for each site, and the results are reported in Table 1. The majority of values are negative at all sites, both for $w_{\text{raw}}$ and $w_{\text{processed}}$, with proportions consistently exceeding 63 %, while positive values account for only about 27.4–31.5 %. This asymmetry is consistent across all sites and remains largely unchanged after the removal of first-order DVMs, indicating that this feature is robust and not primarily driven by DVM-related variability.

Next, considering the mean values of $w_{\text{processed}}$ as a function of depth (panel b), they remain negative at all depths. The mean vertical structure at the NW, SW, and SE sites is similar, with slightly weaker values between 150 and 250 m and more pronounced negative values between 250 and 370 m. Finally, weaker values are again observed, at least down to approximately 400 m. The structure at the NE site is somewhat different. While the values become weaker between 250 and 370 m at the other sites, they become stronger at this site. Between 250 and 370 m, the values at this site then become weaker again, contrary to

https://doi.org/10.5194/egusphere-2026-3095
Preprint. Discussion started: 12 June 2026


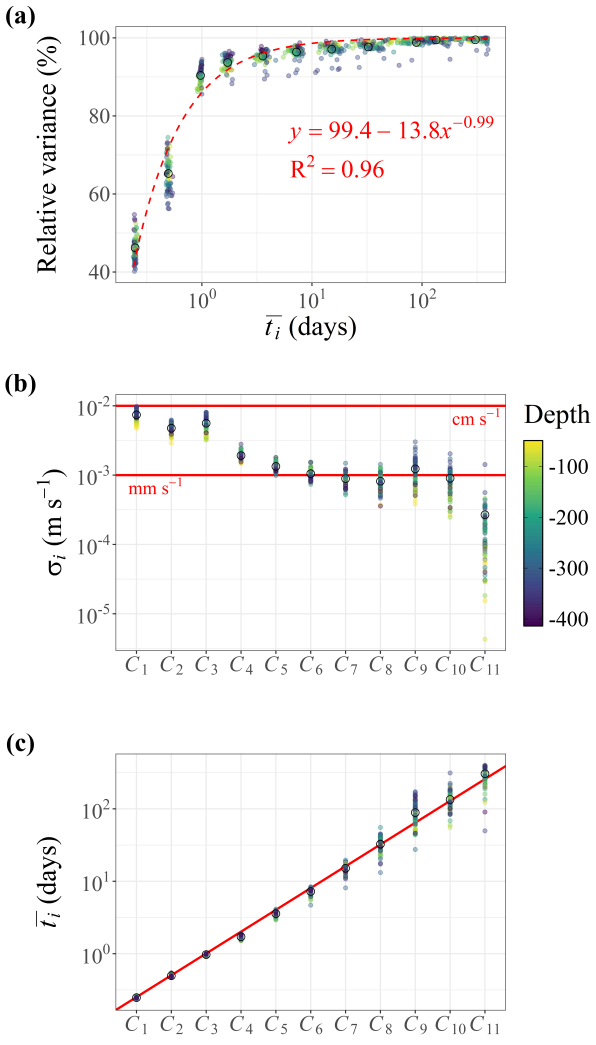


**Figure 6.** Multiscale variability of $w_{\mathrm{raw}}$ from EEMD decomposition. **(a)** Cumulative relative variance as a function of the characteristic time scale $\overline{t_i}$ of each IMF. The dashed line shows the fitted power-law saturation model. **(b)** Standard deviation $\sigma_i$ associated with each IMF. **(c)** Characteristic time scale of each IMF, showing the dyadic relation $\overline{t_i} \sim 2^i$ (red line). Colors represent the depth of the observations, and black dots indicate the mean value of each IMF.

the behavior observed at the two other sites. However, the numerical values remain of the same order of magnitude for all sites (around 3–4 mm s$^{-1}$).

https://doi.org/10.5194/egusphere-2026-3095
Preprint. Discussion started: 12 June 2026


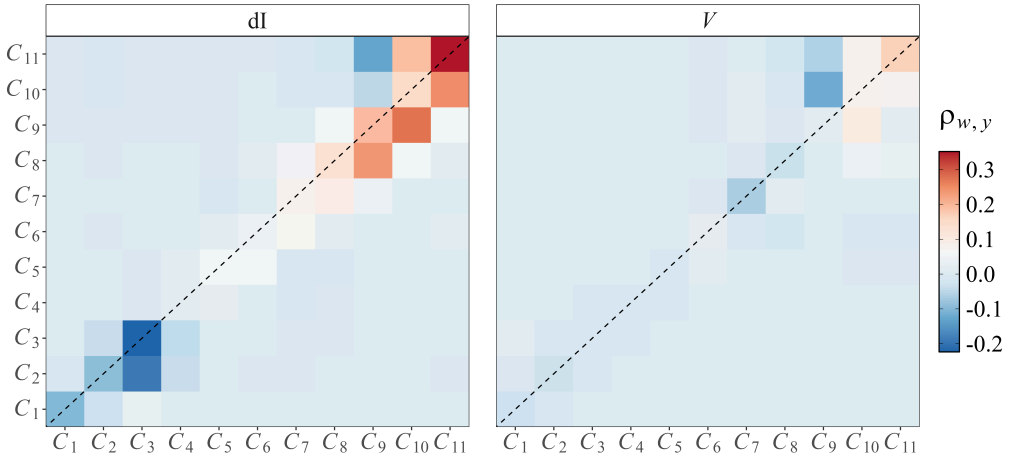


**Figure 7.** Cross-correlation $\rho_{w,y}$ at $\tau = 0$ d between the IMFs $C_i$ of $w_{\mathrm{raw}}$ and those of dI (left panel) and $V$ (right panel).

**Table 1.** Percentage of values above and below $w = 0$ m s$^{-1}$, with ($w_{\mathrm{raw}}$) and without ($w_{\mathrm{processed}}$) first-order DVMs. Values equal to 0 are not counted.

| | $w_{\mathrm{raw}}$ | | $w_{\mathrm{processed}}$ | |
|---|---|---|---|---|
| Site | $w > 0$ | $w < 0$ | $w > 0$ | $w < 0$ |
| Global | 30.9 | 63.6 | 28.7 | 65.4 |
| NE | 31.5 | 63.3 | 30.0 | 64.7 |
| NW | 31.4 | 63.1 | 29.3 | 64.9 |
| SE | 30.6 | 63.8 | 28.3 | 65.7 |
| SW | 30.0 | 64.2 | 27.4 | 66.4 |

## 3.2 Multiscale variability

### 3.2.1 Fourier spectra

Fourier spectra of $w_{\mathrm{raw}}$, weighted by the variance according to the Parseval–Plancherel theorem, are shown in Figure 4. These spectra were smoothed using a decade averaging, since raw Fourier spectra are often quite noisy due to the limited number of data points. The spectra are generally similar regardless of the depth or the site considered. Strong peaks are visible at the 1-day timescale. These peaks correspond to the solar cycle timescale and are related to the cycle of biological vertical movements. They are stronger at depth than at the surface and are more intense at the SW, NW, and SE sites. This daily peak is accompanied by subharmonics, notably at 12 hours, 8 hours, and 4 hours. A broad peak is also observed at the annual scale ($\simeq f^{-2.56}$ d$^{-1}$), again more pronounced at the NW and SE sites than at the NE site. However, this cycle should be interpreted with discretion.

https://doi.org/10.5194/egusphere-2026-3095
Preprint. Discussion started: 12 June 2026


The finite length of the time series limits the reliability of the extracted information at low frequencies, specifically below $f = 10^{-2.25}$ d$^{-1}$, corresponding to long periods ($\approx 180$ days) for which only about two cycles are captured over the duration of the record.

The spectra were estimated again after excluding data categorized as first-order DVMs. Since the spectra were very similar regardless of site or depth, only a global mean spectrum (all depths and sites combined) was considered. In addition, the spectrum of the acoustic backscatter echo intensity dI from the ADCPs (related to the concentration of particles in the water) and the spectrum of the horizontal velocity $V = \sqrt{u^2 + v^2}$ were also estimated. These spectra are presented in panel (a) of Figure 5. When comparing the spectra of $w$ with ($w_{\mathrm{raw}}$) and without ($w_{\mathrm{processed}}$) the first-order DVMs, differences can be observed in the peaks. The diurnal peak is still present in the spectrum of $w_{\mathrm{processed}}$ but it is less pronounced than for $w_{\mathrm{raw}}$. The associated subharmonics are also reduced. This diurnal peak and its subharmonics are also visible in the spectrum of dI. A diurnal peak is also visible in the spectrum of $V$, but it is weaker and not associated with the same subharmonics. This highlights the role of biological processes in the presence and strength of these peaks. Hourly averages of $w_{\mathrm{raw}}$ and $w_{\mathrm{processed}}$ were computed and are shown in panel (b) of the same figure. It is clear that although most of the DVMs have been removed, a biological signal remains in the time series. This signal is cyclic and close to a sinusoidal shape around the mean value. For $w_{\mathrm{processed}}$, the amplitude of this cycle reaches approximately 9 mm s$^{-1}$, amounting to 2.5 times the series mean ($\simeq 3.5$ mm s$^{-1}$). This underscores its prominent role in driving the temporal dynamics.

The spectral scalings were also estimated (see panel a). The spectrum of $V$ follows a slope of $\beta = 1.13$ between approximately 1.5 days ($f \simeq 10^{-0.2}$ d$^{-1}$) and 16 days ($f \simeq 10^{-1.2}$ d$^{-1}$), and a slope of $\beta = 0.37$ between 16 days and 250 days ($f \simeq 10^{-2.4}$ d$^{-1}$). For the spectra of $w$, a slope close to $\beta = 1/3$ ($\beta = 0.4$ for $w_{\mathrm{raw}}$ and $\beta = 0.3$ for $w_{\mathrm{processed}}$) is found for both spectra between 1.6 days and 63 days ($f \simeq 10^{-1.8}$ d$^{-1}$).

### 3.2.2 EEMD analysis

The EEMD analysis was applied to the time series of $w_{\mathrm{raw}}$. This analysis cannot be directly applied to $w_{\mathrm{processed}}$ due to the presence of too many missing data, which are distributed in a non-random manner. This analysis decomposed the time series into 11 IMFs (Intrinsic Mode Functions). The variance of each IMF was estimated and a characteristic time scale was associated with each component using Fourier spectral analysis.

The results are presented in Figure 6. Panel (a) shows the cumulative relative variance as a function of scale, computed for IMF $i$ as follows:

$$RV_i = 100 \cdot \frac{\sum_{k=1}^{i} \sigma_k^2}{\sum_{k=1}^{n} \sigma_k^2 + \sigma_n^2}, \tag{13}$$

where $\sigma_n^2$ denotes the variance of the residual $r_n$. This calculation quantifies the relative contribution of IMFs 1 to $i$ with respect to the total variability represented by all IMFs 1 to $n$. This analysis shows that the majority of the variability in the $w_{\mathrm{raw}}$ time series is contained at small scales equal to or shorter than 1 day, regardless of the site considered or the depth. On average, these scales account for about 90 % of the variance of the time series. The scatter plot follows the form of a power-law relationship. In order to quantify this behavior, an asymptotic saturation model was fitted to the data. This model can be written

https://doi.org/10.5194/egusphere-2026-3095
Preprint. Discussion started: 12 June 2026


as $y = a - bx^{-c}$, where $x$ represents the considered time scale and $y$ the cumulative variance. The parameter $a$ corresponds to the asymptotic value toward which the cumulative variance converges as the scale increases, while $b$ controls the amplitude of the deviation from this limit and $c$ describes the rate of convergence toward saturation. Here, the parameters $a = 99.4$ %, $b = 13.8$ % d$^{-0.99}$ and $c = -0.99$ were obtained ($R^2 = 0.96$). The exponent $c = -0.99$ indicates that the relationship closely follows a $x^{-1}$ scaling, reflecting a rapid decrease in the marginal contribution of increasing temporal scales. Consequently, most of the variance is captured at small scales, while larger scales contribute increasingly marginally. This model reproduces the observed behavior: a rapid increase of explained variance at small scales followed by a progressive slowdown as the scale increases, eventually approaching the total variance of the signal.

Panels (b) and (c) of Figure 6 show the standard deviation and the characteristic scale of each IMF. Overall, the fluctuations of $w_{\mathrm{raw}}$ are on the order of $10^{-2}$–$10^{-3}$ m s$^{-1}$ for scales shorter than 10 days, and below $10^{-3}$ m s$^{-1}$ at larger scales. Finally, it can be noted that the IMFs follow a relationship $\overline{t_i} \sim 2^i$ (see panel c), meaning that the period of an IMF is approximately twice that of the preceding one, reflecting the fact that the EEMD behaves as a dyadic filter. This behavior has previously been reported, for example, for fractional Gaussian noise (Flandrin et al., 2004; Flandrin and Gonçalvès, 2004) or turbulent velocity time series (Huang et al., 2008). This also partly explains why the maximum number of IMFs found is 11: it corresponds to a limit imposed by the size of the dataset (4,272 observations; $\log_2(4272) \simeq 12.04$).

The EEMD analysis was also applied to the time series of the echo intensity anomaly dI and the horizontal velocity $V$. The same number of IMFs was obtained for these variables as for $w_{\mathrm{raw}}$. A comparison between the IMFs of $w_{\mathrm{raw}}$ and those of dI and $V$ was performed using the cross-correlation function evaluated at a lag $\tau = 0$ d. The results of this comparison are presented in Figure 7. Correlations are found for some IMFs of $w_{\mathrm{raw}}$ and dI. In particular, a link is observed for the IMFs $C_3$ of both series, which correspond to the daily cycle in the series (see panel c of Figure 6). This link is not observed between the time series of $w_{\mathrm{raw}}$ and $V$, suggesting a biological origin. Another link is observed between the IMFs $i = 9$ to $i = 11$ of dI and $w_{\mathrm{raw}}$. These IMFs correspond to time scales ranging from about 100 days to 1 year. They therefore reveal a common dynamics between dI and $w_{\mathrm{raw}}$ at these scales. Once again, this link is not particularly observed with $V$, suggesting rather a biological influence.

### 3.3 Rare events recorded

The value of long-term high-frequency monitoring also lies in its ability to detect rare events of a variable relative to its distribution. In this study, we focus on the relationship between $w$ and $u_{\mathrm{cross}}$. A 1-day moving average was applied to both series to retain only fluctuations on time scales longer than a day (thus excluding DVMs). The PDF ratio was then estimated from these filtered series and is shown in panel (a) of Figure 8. This ratio indicates that the two variables are mostly independent. However, strongly positively dependent values ($Q > 1.1$) appear for positive $w$ and $u_{\mathrm{cross}}$. In this range, $Q$ reaches values up to 4.1, indicating that the simultaneous occurrence of these events is 12,500 times more likely than if they occurred independently. These events are rare, as illustrated in panel (b) of the same figure, representing only 0.04 % of the data, and correspond to $u_{\mathrm{cross}}$ above the 99$^{\mathrm{th}}$ percentile and $w$ above the 90$^{\mathrm{th}}$ percentile (after applying the moving average).

https://doi.org/10.5194/egusphere-2026-3095
Preprint. Discussion started: 12 June 2026


During these events, $w$ being positive with some of the highest values encountered, one could be tempted to call them strong upwelling events associated with shoreward-directed currents. While these events were recorded at the SW site, they were not observed with the same amplitude at the other three sites. Two periods were identified: the first during the austral autumn between 15 and 16 March 2024 (UTC), and the second during the austral summer between 7 and 9 February 2025 (UTC). These periods were isolated, and the mean $w$, $v_{\mathrm{along}}$, and $u_{\mathrm{cross}}$ profiles were calculated (Figure 8; panels c, d, and e). The mean state (black lines) exhibits negative velocities. In contrast, during these events (blue lines), the flow displays a strongly sheared vertical structure. In the upper 200 m, a surface-intensified negative along-shore jet develops, reaching up to $-0.4$ m s$^{-1}$. The cross-shore velocity is positive throughout this layer, indicating onshore transport towards the coast. Meanwhile, the vertical velocity $w$ is positive, with values up to 6 mm s$^{-1}$. Below 200 m, a marked transition occurs. All velocities reverse signs. The along-shore velocity weakens and reverses, as well as the cross-shore velocity which also becomes negative, indicating offshore transport between 250 and 400 m depth. At the same depths, the vertical velocity becomes strongly negative, reaching approximately $-5$ mm s$^{-1}$ at 330 m.

To further illustrate the temporal dynamics of these phenomena, Figure 9 presents the time series surrounding the March 2024 upwelling event. Panel (a) describes the ERA5 10-m wind conditions (Hersbach et al., 2020), showing a period of strong winds peaking near 15 m s$^{-1}$ with a direction ($W_d$) predominantly between 300° and 320° prior to the event, corresponding to the trade winds. Approximately at the same time, the 50-m depth temperature drops by 2 degrees, from 25 °C to 23 °C (panel b). Panel (c) shows the 1-day moving average of the vertical velocity $w$. The sharp reversal of the vertical flow (delimited by purple lines), where $w$ rapidly peaks at approximately 7 mm s$^{-1}$, is highly episodic and abrupt. Concurrently, the horizontal flow undergoes a drastic intensification (panel d). The stick plot, derived from the moving averages of $u_{\mathrm{cross}}$ and $v_{\mathrm{along}}$, reveals that this upwelling pulse coincides with a sudden acceleration of the horizontal currents $V$, with velocity magnitudes abruptly exceeding $0.5$ m s$^{-1}$ (indicated by the bright yellow vectors). During this window, the vectors are strongly oriented in the negative along-shore and positive cross-shore directions, visually confirming the intense shoreward-directed jet described previously. Immediately following this event, both vertical and horizontal velocities rapidly drop.

## 4 Discussion

In this study, current velocity data were measured using ADCPs every two hours throughout the water column at four sites offshore of Nouméa over a period of nearly one year. These time series proved to be rich in information and enabled us to characterize the dynamics of vertical velocities, $w$, within this ecosystem. The main results obtained through the analyses performed are summarized in the paragraphs below.

It is nevertheless important to emphasize a key point here before discussing these results: the uncertainty associated with ADCP measurements. The measurement accuracy provided by the manufacturer only applies to horizontal velocities. An error of $\pm 1$ % $\pm 5$ mm s$^{-1}$ is therefore expected for these velocities (corresponding to the most pessimistic case). The accuracy is not directly specified for vertical velocities. However, this measurement is expected to be more precise because it relies on the cosine of the instrument beam angle (20°, in our case) rather than the sine, and because the vertical velocity is derived

https://doi.org/10.5194/egusphere-2026-3095
Preprint. Discussion started: 12 June 2026


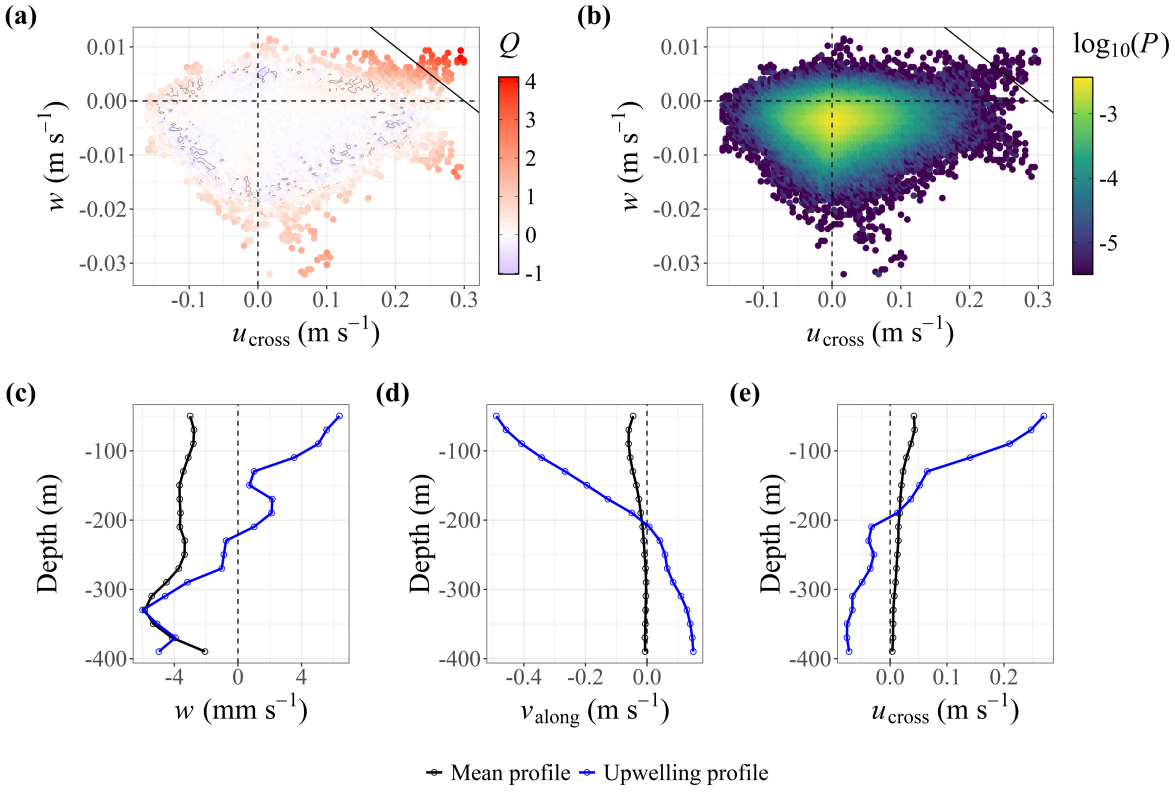


**Figure 8.** **(a)** PDF of the ratio $Q$ and **(b)** 2D joint PDF of $w$ and $u_{\text{cross}}$, both smoothed using a 1-day moving average (all sites and depths). The black line indicates the empirical relationship $y = -0.1x + 0.03$, above which a positive dependence is observed. The bandwidths used to calculate the PDFs are equal to 1 % of the difference between the maximum and the minimum value of the considered data set. **(c–e)** Mean vertical profiles at the SW site for (c) $w$, (d) $v_{\text{along}}$, and (e) $u_{\text{cross}}$, also smoothed with a 1-day moving average. Black lines indicate the full dataset, and blue lines correspond to strong upwelling conditions.

from the four beams simultaneously. One may estimate the vertical precision from the horizontal specification using a factor $\sin(20°)/\cos(20°) \approx 0.364$. Thus, assuming a horizontal precision of 0.5 cm s$^{-1}$ (manufacturer specification), the corresponding vertical precision would be approximately 1.8 mm s$^{-1}$. This is probably an overestimated value. Although this uncertainty is not negligible, it does not invalidate the results obtained in this study nor the points discussed in the following sections. Accounting for this uncertainty rigorously remains difficult, since the measurement error is not linear. Nevertheless, it is important to keep these limitations in mind throughout the analysis.

https://doi.org/10.5194/egusphere-2026-3095
Preprint. Discussion started: 12 June 2026


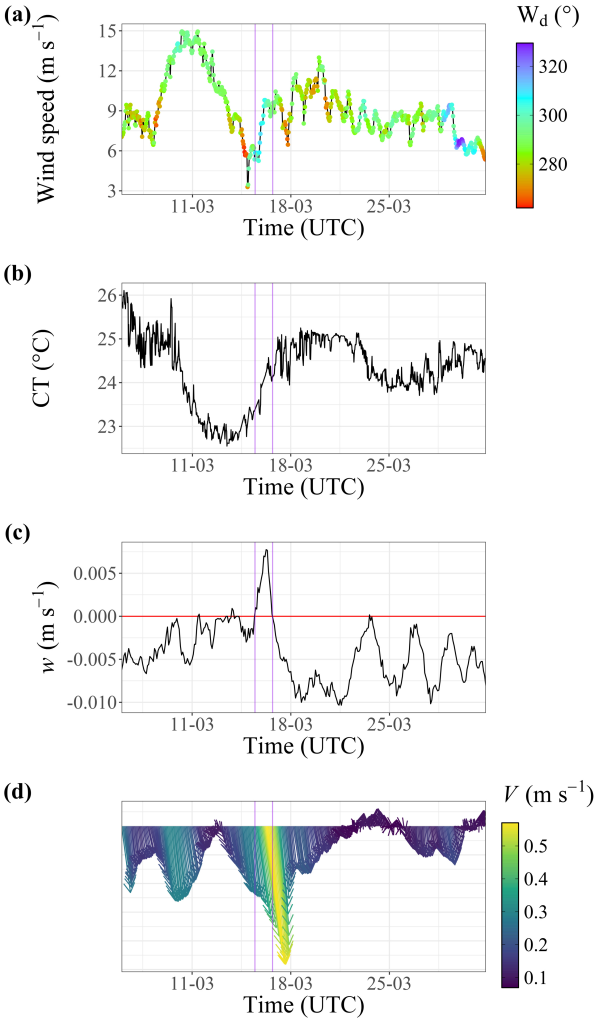


**Figure 9.** **(a)** ERA5 10-meters wind data (Hersbach et al., 2020), **(b)** conservative temperature (CT) from the RBR© sensor at 50 m depth, **(c)** 1-day moving average of $w$ and **(d)** stick plot of $u_{\text{cross}}$ and $v_{\text{along}}$ (also smoothed using a moving average) over the period from 6 to 31 March 2024 at 50 m depth. A displacement of the arrows along the $x$ axis indicates a variation in $u_{\text{cross}}$, while variations along the $y$ axis indicate a variation in $v_{\text{along}}$. The color represents the horizontal velocity. The vertical purple lines indicate the period from 15 March (starting at 12:00 h UTC) to 16 March 2024 (ending at 16:00 h UTC), corresponding to the upwelling period.

### 4.1 Weak global downwelling circulation

340 The Alis Current of New Caledonia (ACNC) flows southeastward along the western coast of the island, which characterizes a left-bounded coastal flow in the Southern Hemisphere. Away from the canyons, the along-shore flow is in (quasi-)geostrophic balance at a large scale. Diminished Coriolis force (directed onshore) or increased pressure gradient force (offshore) can favor

https://doi.org/10.5194/egusphere-2026-3095
Preprint. Discussion started: 12 June 2026


downwelling conditions on the shelf slope. Here vertical velocities exhibit a systematic negative average ($w < 0$, indicating downwelling) that is probably favored by the submarine topography (see Figure 1), disrupting the geostrophic balance, following the mechanisms described by Klinck (1996) and briefly summarized here. Indeed, as the ACNC flows over the submarine canyons, the along-shore velocity ($v_{\mathrm{along}}$) is reduced due to interactions with the canyon walls and increased bottom friction. Because the Coriolis force $F_c$ is proportional to velocity (with magnitude $f_c v$, where $f_c$ is the Coriolis parameter), this local deceleration leads to a weakened Coriolis force within the canyons. Consequently, the offshore pressure gradient force remains unbalanced. This uncompensated gradient drives an offshore-directed flow at depth. To satisfy mass conservation, this localized offshore transport forces the overlying water column downward, leading to downwelling. Therefore, the average negative vertical velocity values observed in our results are consistent with the topographically-induced downwelling regime expected for a left-bounded flow in the Southern Hemisphere. Moreover, applying the incompressible continuity equation between our sites lead to the nullity of the velocity divergence, such that:

$$\frac{\partial w}{\partial z} = -\frac{\partial u}{\partial x} - \frac{\partial v}{\partial y} \tag{14}$$

Under strong assumptions, we were able to estimate theoretical vertical velocities of $-0.09$ mm s$^{-1}$ at 50 m, and $-0.008$ mm s$^{-1}$ at 100 m. This is consistent with the presence of a downwelling in the study area.

This topographic control is further supported by the numerical findings of Spurgin and Allen (2014), who demonstrated that submarine canyons significantly enhance downward advection in downwelling-favorable regimes. Their study shows that the magnitude of this vertical flux is primarily driven by the Burger number (stratification) and the Rossby number (flow intensity). Specifically, they found that higher Rossby numbers—corresponding to stronger along-shore currents like the ACNC—lead to more intense negative vertical fluxes at the shelf break depth. We estimated the Rossby and Burger numbers, which respectively characterize the relative importance of rotational effects and stratification in the flow. The dimensionless Rossby number is estimated as follows:

$$Ro = \frac{V}{f_c L} \simeq 0.06 \tag{15}$$

where $V = 0.1$ m s$^{-1}$ is the mean horizontal velocity, and $L = 3\times10^4$ m is the characteristic length of the surrounding canyons. At our latitude, the Coriolis parameter is $f_c = 2\Omega \sin\phi = 5.58 \times 10^{-5}$ rad s$^{-1}$, where $\Omega = 7.2921 \times 10^{-5}$ rad s$^{-1}$ is the angular speed of Earth's rotation and $\phi$ is the latitude (in radians). The Burger number can be estimated according to the following formula:

$$Bu = \left(\frac{NH}{f_c L}\right)^2 \simeq 9.8 \tag{16}$$

where $H = 500$ m is the characteristic depth at our sites, and $N = 0.01$ s$^{-1}$ is the Brunt-Väisälä frequency, estimated empirically from RBR© sensors data (see the location of the mooring in Figure 1) between 14 m and 463 m, as follows:

$$N = \sqrt{-\frac{g}{\rho_0}\frac{\partial \rho}{\partial z}} \tag{17}$$

https://doi.org/10.5194/egusphere-2026-3095
Preprint. Discussion started: 12 June 2026


where $g = 9.81\ \mathrm{m\ s^{-2}}$ is the acceleration due to gravity, $\rho_0 = 1025\ \mathrm{kg\ m^{-3}}$ is the reference potential density of seawater, $\rho$ is the density, and $z$ is the depth. The density was estimated using conservative temperature and absolute salinity (Figure 10), following the TEOS-10 equation of state (see McDougall, 2026 for more details). Note that in Spurgin and Allen (2014), the Burger number corresponds to the square root of the above definition. The combined analysis of the dimensionless Rossby ($Ro \simeq 0.06$) and Burger ($Bu \simeq 9.8$) numbers reveals a marine environment that is both highly energetic and strongly constrained by its vertical structure. This is further reflected in the low Froude number, $Fr = Ro/\sqrt{Bu} \simeq 0.02$, which is characteristic of flows where rotational and stratification effects jointly dominate (Cushman-Roisin, 1994). Moreover, this abrupt topographic forcing in such a stratified environment is also a recognized driver of internal wave generation (Bell Jr., 1975; Gordon and Marshall, 1976; Petruncio et al., 1998; Allen and Durrieu de Madron, 2009; Baines, 2022).

### 4.2 Multiscale dynamics

Since the time series are sufficiently long, it was possible to investigate their multiscale dynamics from a statistical perspective. First, a Fourier spectral analysis was performed. This analysis revealed a strong similarity in the multiscale dynamics of the time series across the four sites and for the different depths considered.

At first, a spectral slope close to $\beta = 1.1$ was identified for the horizontal velocity over time scales ranging from 1.5 to 16 days. This decay, very close to the theoretical $f^{-1}$ scaling ($\beta = 1$), has already been documented in several previous studies of geophysical flows (e.g., Katul and Chu, 1998; Katul et al., 2012; Renosh et al., 2014; Schmitt and Huang, 2016). The emergence of this power law departs from the classical isotropic inertial cascade ($-5/3$; Kolmogorov, 1941; Obukhov, 1941) and constitutes a characteristic signature of a dynamics strongly constrained by the boundaries, particularly topography. Indeed, at the sub-inertial time scales considered here, the horizontal structures advected by the flow have dimensions much larger than the fluid depth. These large vortical structures therefore strongly interact with the bottom boundary. This geometric confinement, together with the resulting shear, inhibits the development of a homogeneous and isotropic three-dimensional energy cascade. The variance is then redistributed according to an $f^{-1}$ slope, a spectral equilibrium that theory could explain through the action of a Heisenberg eddy viscosity, reflecting the continuous internal damping exerted by smaller scales on these large bottom-sheared structures (Katul et al., 2012). For time scales larger than 16 days (up to at least 250 days), a flatter spectrum is observed, with a spectral slope close to $\beta = 1/3$. This flattening may correspond to the synoptic scales of energy injection into the system, in the sense of Richardson's energy cascade (Richardson, 1922). These scales are, for instance, referred to as the "geostrophic eddy range" (or "synoptic-scale eddy range") by Ferrari and Wunsch (2009), highlighting the presence of large-scale structures generated by processes such as pressure and Coriolis forces, characteristic of geostrophic turbulence at the global scale (Charney, 1971; Stammer, 1997). However, it is worth noting that a weak but non-negligible dynamical signal is still observed at these scales for the vertical velocity component $w$, indicating that these structures are not purely geostrophic, but rather ageostrophic.

In contrast to the horizontal component, the spectrum of the vertical velocity $w$ exhibits a much weaker decay, characterized by a slope of $\beta \approx 1/3$ over a range of scales from 1.5 to 63 days. This reduced spectral attenuation highlights the fundamental anisotropy of the flow. Indeed, stratification and geometric confinement strongly suppress the development of large vertical

https://doi.org/10.5194/egusphere-2026-3095
Preprint. Discussion started: 12 June 2026


motions at low frequencies, a classical decoupling in confined geophysical flows (Katul et al., 2012). As a result, the variance of the vertical velocity is distributed much more uniformly across the frequency band. This behavior reflects the signature of a field dominated by internal gravity waves. The canonical model of Garrett and Munk (1979) predicts a theoretically flat temporal spectrum ($\beta = 0$) for this component, while other approaches based on the conversion of spatial spectra suggest a theoretical slope around $\beta = 0.5$ (Klymak and Moum, 2007a). The observed decay of $\beta = 0.4$ for $w_{\mathrm{raw}}$ (and $\beta = 0.3$ for $w_{\mathrm{processed}}$) therefore falls well within this expected range, suggesting an intermediate regime in which wave propagation and nonlinear energy transfers coexist. The slight deviation from purely linear equilibria may be explained by the presence of nonlinear wave–wave interactions or by local intermittency of turbulence (e.g., Polzin and Lvov, 2011; D'Asaro et al., 2007; D'Asaro, 2014).

A first element of insight into intermittency can be provided here. Indeed, if one considers the expected scaling of the first-order structure function $\langle \Delta_\tau X \rangle \sim \tau^H$ (not shown here), where $\Delta_\tau X = |X(t+\tau) - X(t)|$, the Hurst exponent $H$ can be estimated. This exponent describes how the temporal increments of the series evolve with the considered time scale. For the mean structure function of $w$, a value $H = -0.28$ is obtained using the Extended Self Similarity method (used here to reduce the effect of periodicities on the scaling; Benzi et al., 1993). Negative values of $H$ are not commonly observed, but they have already been reported in previous studies (e.g., Lovejoy and Schertzer, 2012, 2013; Renosh et al., 2015; Schmitt and Huang, 2016). This indicates that small-scale fluctuations are larger than large-scale ones and dominate the dynamics of the time series. From these values of $H$ and $\beta$, an intermittency indicator can also be derived as $\mu = 2H - (\beta - 1)$. For a non-intermittent series, $\mu = 0$ (Kolmogorov, 1962), and $\mu > 0$ if the series is intermittent (i.e., there are extremes at different scales in the series). For the $w$ series, a mean value $\mu = 0.04$ can be estimated. This value is close to what can typically be expected for velocities or passive scalars in turbulence (Schmitt, 2006; Robache et al., 2025). This indicates that the series are multifractals.

However, our results (and particularly those concerning intermittency) should be interpreted with a certain degree of nuance. As seen previously, the $w$ data are not purely driven by physics, but are biased by biological movements. For the signal to be purely physical, the particles detected by the ADCPs would need to be strictly passive. However, our data are "contaminated" by the active behavior of certain small organisms. This was highlighted, for example, by the Fourier spectral analysis, where a diurnal peak associated with various sub-harmonics was observed. Furthermore, it is likely that these biological peaks mask other physical periodicities in the time series, such as the semi-diurnal tide (M2 wave with a 12.4 h period) and the lunisolar declination tide (K1 wave with a 24.96 h period), which are observed in the horizontal velocity $V$ (see Figure 5), and the sea surface height in our study area (Bendinger et al., 2023, 2025). In practice, it is difficult to separate the physical and biological components of the measured $w$. Here, a method was tested to at least provide an indication of the origin of the observed phenomena: the Ensemble Empirical Mode Decomposition (EEMD). Through this analysis, it was highlighted that biological effects are mainly expected at the diurnal and seasonal scales. Moreover, these two scales are also found in the Fourier spectra of $w$, in the form of more or less localized peaks. The diurnal influence is due to the daily migrations of these small organisms, aligned with the solar cycle (Cohen and Forward Jr., 2009; van Haren and Compton, 2013; Clements et al., 2026). It was noted here that even when removing the highest values associated with these migrations (on the order of cm $s^{-1}$), a diurnal component persists. This could therefore indicate that, although intense active migration phases can be

https://doi.org/10.5194/egusphere-2026-3095
Preprint. Discussion started: 12 June 2026


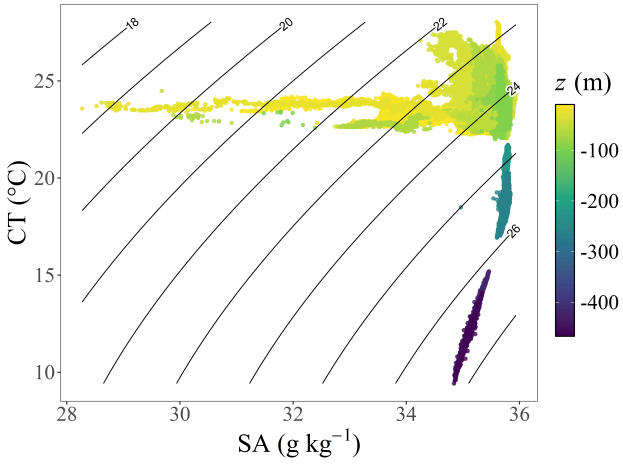


**Figure 10.** Temperature-Salinity (T-S) diagram (conservative temperature versus absolute salinity) of the data recorded by the RBR© sensors.

identified, these organisms nevertheless move throughout the day. The seasonal influence, on the other hand, is possibly linked to several factors. First, DVMs almost certainly possess their own multiscale dynamics that are embedded within the $w$ series, and seasonal effects could therefore be expected in connection with, for example, plankton bloom periods. However, two other factors could also be at the origin of this seasonality: our sampling time step, which causes us to sample at varying temporal distances from the exact time of sunset or sunrise (see Figure 2d), thereby sometimes sampling the core of the migration or its end (and in a dissimilar manner between sunrise and sunset); and a potential non-linear effect of these migrations on the ADCP bias. Indeed, it cannot be ruled out that the higher the abundance of these organisms, the stronger the biases will be (due to their patchiness, in particular). This observation also raises an important point regarding the optimal sampling frequency for DVMs, which must be high enough to mitigate these issues.

The link between the dI and $w$ series is certainly non-linear, but it nevertheless offers an interesting perspective for attempting to separate the physical and biological components of $w$. The analyses could be further developed in this direction in other studies (particularly for sites also equipped with echosounders), to observe how this relationship between the series evolves over time. To do this, the time-dependent intrinsic correlation method, based on EMD (Chen et al., 2010), could be used to obtain initial insights. This method has already highlighted relationships between time series in oceanography, for example between temperature and oxygen (Huang and Schmitt, 2014), or between temperature series at different locations (Kbaier Ben Ismail et al., 2015; Derot et al., 2016).

### 4.3 Episodic upwellings

In this study, the PDF quotient analysis was used to identify rare events (i.e. infrequently observed values) highlighting dependencies between the distributions of different variables. A dependence between relatively high positive values of $w$ and $u_{\mathrm{cross}}$ was identified. These events, which can be classified as strong upwelling events (relative to the mean dynamical state of the

https://doi.org/10.5194/egusphere-2026-3095
Preprint. Discussion started: 12 June 2026


study area), were further investigated. First, these strong upwelling events were not observed at all four sites, but only at the SW site. During the year of study, these events were observed twice and only lasted a few days. Longer time series would obviously be needed to check whether these episodic events occur every year, and at which frequency. Yet, this does not imply that the other sites do not respond to the forcing responsible for these upwellings. Indeed, values of $w$ remain negative at the other sites, but are closer to zero compared to their mean state. Rather, this suggests that each site exhibits a distinct response, particularly in terms of amplitude. The difference between the responses is sufficiently large to modify the interpretation of the observed event (i.e., upwelling or downwelling), despite the sites being separated by only a few kilometers (between 1.8 and 2.7 km). This highlights a strong small-scale spatial heterogeneity in the vertical velocity response, at least during these rare events. Second, these strong upwelling events are primarily confined to the upper 200 m of the water column. A reversal in the sign of both $u_{\mathrm{cross}}$ and $v_{\mathrm{along}}$, relative to their typical values, is observed below this depth. This suggests the presence of two oppositely directed flows within the water column, potentially inducing strong vertical shear and the development of two distinct overturning cells. The upper cell (above approximately 200 m) is characterized by a strong horizontal flow (exceeding $0.4\,\mathrm{m\,s^{-1}}$) directed onshore and southeastward. Within this layer, $w$ exhibits positive values ($w > 0$) opposite to the mean state, consistent with upwelling conditions. In contrast, the deeper cell is characterized by weaker values of $u_{\mathrm{cross}}$ and $v_{\mathrm{along}}$, flowing in the opposite direction. The current is directed offshore and northwestward. At this stage, the *in situ* available variables do not allow us to fully explain the mechanisms driving this structure. However, the observed upwelling is likely associated with a vertically sheared along-shore current and a secondary cross-shore circulation, suggesting that processes beyond classical Ekman dynamics, such as baroclinic adjustment, topographic effects, or frontal dynamics, may play a significant role. Complementary satellite-derived observations suggest that these strong upwelling events at the SW site coincide each time with the passage of a large cyclonic circulation offshore of the island, migrating from South to North, and reinforcing the ACNC along the coast (see Appendix A for more details). At the same time, a strong 12-hour periodicity is observed in the horizontal velocity data, as well as in the depth data from the RBR© sensors (with amplitudes reaching up to 30 m). These features could be the source of the intensified horizontal velocities, potentially triggering topographically-induced upwelling (shelf-break upwelling; Kämpf and Chapman, 2016) and internal tides. Under these conditions, the strong currents along the topographic slope may overcome the otherwise downwelling average condition, ultimately resulting in the observed upward vertical motion.

Note that the strong trade winds were concomitant with the drop in surface temperature (about 2 °C) and reduction of the ACNC signal (see Figure 9) corresponding to the description of wind-driven coastal upwellings, well described in the literature (Ganachaud et al., 2010). While, in our data, the episodic strong positive $w$ studied here occurs after the strong trade winds while temperature starts warming again. Such vertically structured circulation, characterized by the coexistence of oppositely directed flows and enhanced shear, has already been reported in coastal systems and is often associated with the presence of overturning secondary circulation and topographic effects (Song and Chao, 2004; Relvas and Barton, 2005; Kämpf, 2017; Chen et al., 2023). Finally, it should be noted that the present analysis focuses exclusively on strong upwelling events. Other upwelling occurrences (of weaker intensity), potentially related to the regional dynamics previously described by Alory et al. (2006), Ganachaud et al. (2010), and Marchesiello et al. (2010), may also be present in the $w$ time series, but are not considered here. A dedicated study would be required to fully characterize their properties and underlying dynamics.

https://doi.org/10.5194/egusphere-2026-3095
Preprint. Discussion started: 12 June 2026


This would be particularly valuable, as episodic upwelling events occurring within predominantly downwelling regions may exert significant impacts on local biogeochemical processes (e.g., Hanson et al., 2005).

## 5 Conclusions

In this study, year-long ADCP measurements collected at high temporal and vertical resolution provided new insights into the dynamics of vertical velocities in a marine environment influenced by complex bathymetry offshore New Caledonia. Year-wise, the vertical velocity field is dominated by persistent downwelling (3–4 mm $s^{-1}$), consistent with a canyon-induced mechanism resulting from the disruption of geostrophic balance as the along-shore current interacts with steep topography. At smaller temporal scales, the analysis reveals a rich multiscale dynamics. The horizontal velocity exhibits a characteristic $f^{-1}$ spectral slope, reflecting the strong influence of topographic confinement and bottom shear on the flow. In contrast, the vertical velocity displays a much flatter spectrum ($f^{-0.4}$ slope), consistent with a regime dominated by internal wave dynamics and anisotropic turbulence. The intermittency analysis further suggests that vertical motions are governed by multifractal dynamics, although the interpretation of these results must be nuanced due to the influence of biological processes. Beyond this mean and statistical description, the identification of rare events highlights the presence of intense and spatially heterogeneous upwelling episodes. These events are confined to specific locations and are associated with vertically structured flows characterized by strong shear and the coexistence of oppositely directed currents. Such structures point toward the importance of secondary circulation, internal tides, baroclinic processes, and topographic interactions, extending beyond the classical Ekman framework. Overall, this study emphasizes that the vast majority of vertical velocity variability unfolds at small temporal scales. Consequently, these motions cannot be interpreted solely through large-scale or mean dynamics. Instead, they emerge from the interplay between topography, stratification, multiscale variability, and episodic processes. Ultimately, characterizing these complex vertical motions provides a critical foundation for understanding regional biogeochemistry. In this environment where primary productivity is fueled by diazotrophic cyanobacteria (through $N_2$ fixation), such multiscale physical dynamics are likely key drivers of both the supply of limiting nutrients and the subsequent export of carbon to the deep ocean. In this context, future studies should combine high-frequency measurements of vertical velocity with simultaneous observations of organic matter export to better quantify the impact of vertical velocity on the biological carbon pump. Moreover, future work should aim at better disentangling the physical and biological contributions to the measured vertical velocities, for instance through combined acoustic and optical observations. In addition, higher-resolution and higher-frequency observations would allow for the exploration of other scaling regimes for $w$ (e.g., Klymak and Moum, 2007b; van Haren, 2008, 2015) in this region. Together with numerical simulations, they would be highly valuable to further investigate the mechanisms driving the observed episodic upwelling events and their role in vertical exchanges and ecosystem functioning.

https://doi.org/10.5194/egusphere-2026-3095
Preprint. Discussion started: 12 June 2026


## Appendix A: Additional SPASSO and SWOT analyses of the March 2024 upwelling event

To provide additional context on the large-scale cyclonic circulation associated with the strong upwelling events identified in the main analysis (March 2024 example), DUACS L4 satellite-derived products computed with the SPASSO software (Rousselet et al., 2025) were examined. In particular, absolute dynamic topography (ADT) and surface geostrophic currents were used to characterize the regional ocean dynamics around the study area. Figure A1 shows the temporal evolution of ADT and associated surface circulation on 4, 16, and 30 March. On 4 March (panel a), the cyclonic circulation, southwest of the area of study, is relatively weak, with no clear signature of coastal anomalies. On 16 March (panel b), the cyclonic circulation is strongly reinforced (ADT weakening) west and northwestward of Nouméa. This structure coincides with a strengthening of the surface currents and enhanced gradients in ADT near the coast, particularly in the vicinity of the study area. By 30 March (panel c), the low-ADT region has kept on intensifying and expanding northwestward. The persistence of this structure suggests the development and propagation of a consistent mesoscale cyclonic feature offshore of the island. Considering the low resolution of L4 gridded data (DUACS product) and poor reliability near the coast, the presence and precise location of the cyclonic feature is investigated using higher resolution SWOT L3 observations available in March 2024 in our study area. These observations are shown in Figure A2. The cyclonic structure, represented by the blue patch, is located to the south of the study area on 8 March (panel a), then farther northwest on 19 March and 29 March (panels b and c). Hence the study area is influenced by a transient cyclonic circulation during mid-March, which may contribute to the modification of the local flow field and enhance along-shore velocities,as mentioned in the article.

*Code and data availability.* The mooring velocity data are freely available online (Petrenko et al., 2026). The bathymetric data used in this study are publicly available (0.001° resolution; SHOM-IRD, 2021). The SWOT (Level-3 KaRIn Low Rate SSH Expert v3.0, CNES, https://doi.org/10.24400/527896/A01-2023.018; AVISO/DUACS, 2025b) and DUACS (global Level-4 gridded data, Copernicus Marine Service, https://doi.org/10.48670/moi-00148; AVISO/DUACS, 2025a) products are freely available online. The Python code for Fourier spectral analysis was developed by Gao et al. (2021b) and is available on GitHub (Gao et al., 2021a). The R code used for probability density function (PDF) estimation and PDF quotient analysis is also available on GitHub and Zenodo (Robache and Schmitt, 2025b). The R packages tidyverse (Wickham and RStudio, 2023), Rlibeemd (Helske and Luukko, 2025), and gsw (Kelley et al., 2024) were used in this study.

*Author contributions.* KR: Conceptualization, Formal analysis, Methodology, Visualization, Writing – original draft, Writing – review & editing; AAP: Conceptualization, Methodology, Supervision, Resources, Funding acquisition, Writing – review & editing; MG: Investigation, Data Curation, Writing – review & editing; LR: Investigation, Data Curation, Writing – review & editing; SB: Investigation, Data Curation, Writing – review & editing.

*Competing interests.* The authors declare that no competing interests are present.

https://doi.org/10.5194/egusphere-2026-3095
Preprint. Discussion started: 12 June 2026


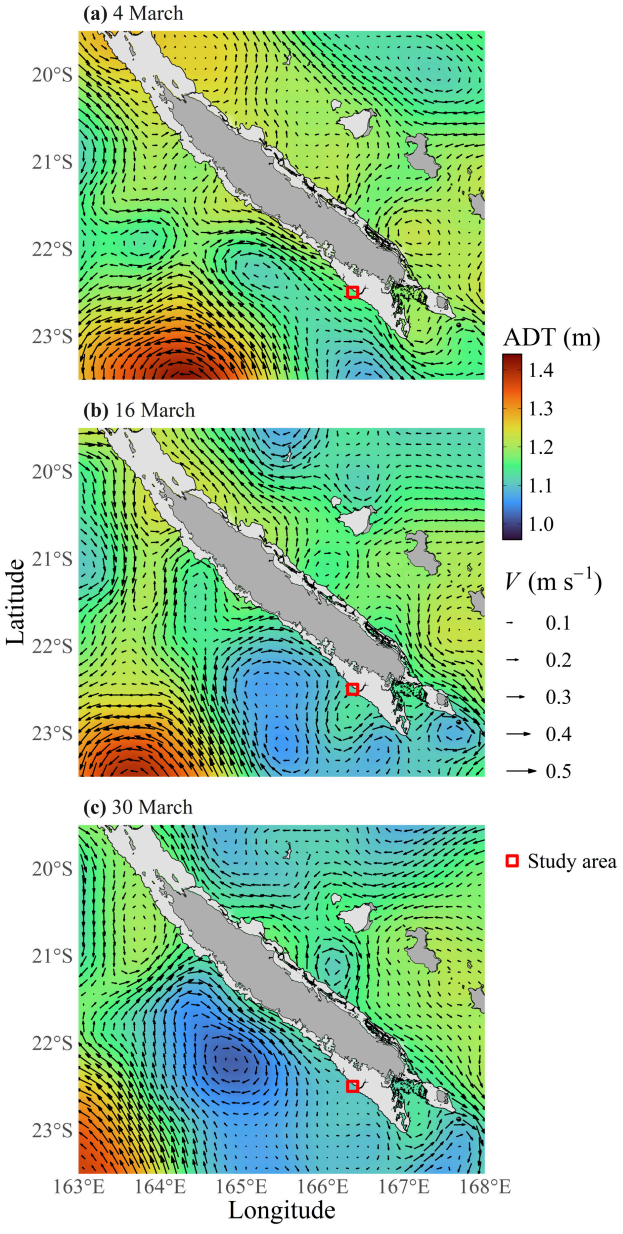


**Figure A1.** Temporal evolution of absolute dynamic topography (ADT) and surface circulation in the vicinity of the study area during March 2024. Panels show conditions on **(a)** 4 March, **(b)** 16 March, and **(c)** 30 March. Colors represent ADT (m), while arrows indicate surface geostrophic currents (m $s^{-1}$) derived from satellite altimetry (DUACS products, SPASSO software; Rousselet et al., 2025). The red square highlights the study area. The grey area represents areas where the depth is less than 50 m, not considered here.

https://doi.org/10.5194/egusphere-2026-3095
Preprint. Discussion started: 12 June 2026


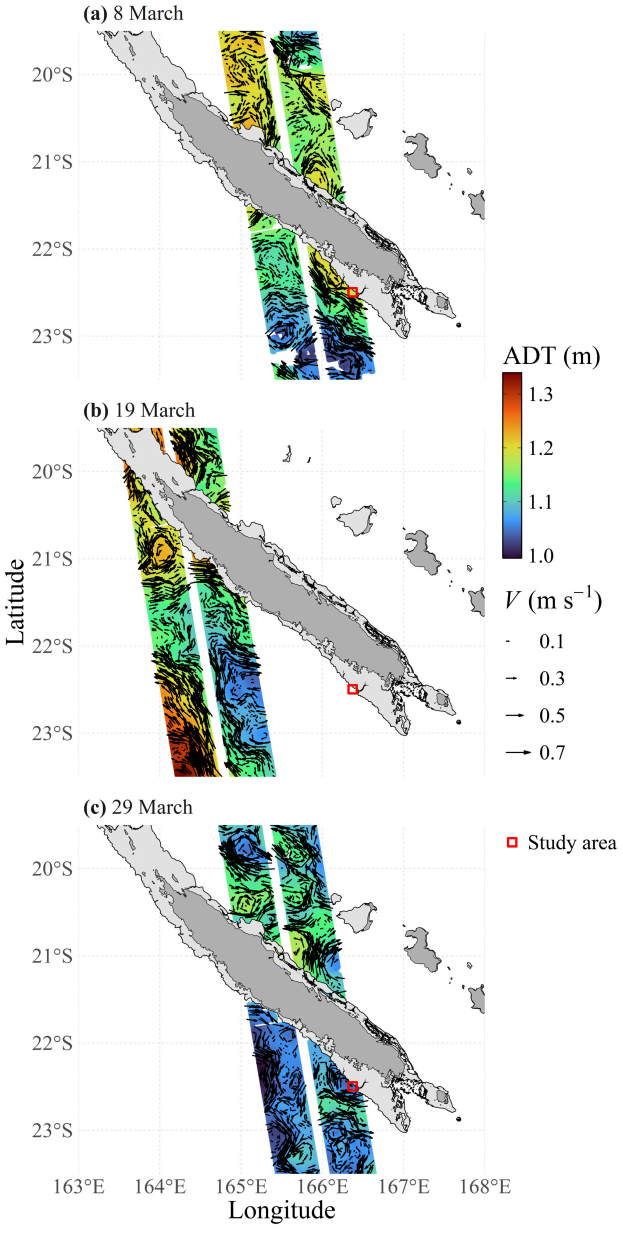


**Figure A2.** Temporal evolution of absolute dynamic topography (ADT) and surface circulation in the vicinity of the study area during March 2024. Panels show conditions on **(a)** 8 March, **(b)** 19 March, and **(c)** 29 March. Colors represent ADT (m), while arrows indicate surface geostrophic currents (m $s^{-1}$) derived from satellite altimetry (SWOT products). The red square highlights the study area. The grey area represents areas where the depth is less than 50 m, not considered here.

https://doi.org/10.5194/egusphere-2026-3095
Preprint. Discussion started: 12 June 2026


*Acknowledgements.* The data valorized in the HOPE-VV project were acquired with the support of the agents (especially Emmanuel de Saint-Léger, Carl Gojak, and Arnaud Le Ridant) and equipment of the Parc National d'Instrumentation Océanographique of the Technical Division of the Institut National des Sciences de l'Univers (INSU) of the Centre National de la Recherche Scientifique (CNRS), of the agents (especially Céline Bachelier and Damien Vignon) of the Instrumentation, Moyens Analytiques, Observatoires en Géophysique et Océanographie (IMAGO) research support unit of the Institut de Recherche pour le Développement (IRD), and of our colleague of the MIO Jean-Luc Fuda. We also thank Loïc Michel from RDI for the discussions regarding the technical specifications of the ADCPs. The 4 moorings were deployed in 2024 during the HOPE-02 cruise (https://doi.org/10.18142/330; Bonnet, 2024) and recovered in 2025 during the HOPE-07 cruise (https://doi.org/10.17600/18003527; Bonnet, 2025). The authors thank the French Government for supporting Kévin Robache through a postdoctoral fellowship within the HOPE-VV project (principal investigator Anne A. Petrenko), funded under the France 2030 investment plan and the Initiative d'Excellence of Aix-Marseille Université (AMidex, grant no. AMX-22-RE-AB-147).

https://doi.org/10.5194/egusphere-2026-3095
Preprint. Discussion started: 12 June 2026


## References

Allen, S. E. and Durrieu de Madron, X.: A Review of the Role of Submarine Canyons in Deep-Ocean Exchange with the Shelf, Ocean Science, 5, 607–620, https://doi.org/10.5194/os-5-607-2009, 2009.

Alory, G., Vega, A., Ganachaud, A., and Despinoy, M.: Influence of Upwelling, Subsurface Stratification, and Heat Fluxes on Coastal Sea Surface Temperature off Southwestern New Caledonia, Journal of Geophysical Research: Oceans, 111, https://doi.org/10.1029/2005JC003401, 2006.

Arnaud, M., Petrenko, A., Fuda, J.-L., Comby, C., Bosse, A., Ourmières, Y., and Barrillon, S.: Estimating Oceanic Physics-Driven Vertical Velocities in a Wind-Influenced Coastal Environment, Ocean Science, 21, 2829–2847, https://doi.org/10.5194/os-21-2829-2025, 2025.

AVISO/DUACS: Global Ocean Gridded L 4 Sea Surface Heights And Derived Variables Reprocessed 1993 Ongoing [Data Set], https://doi.org/10.48670/moi-00148, 2025a.

AVISO/DUACS: SWOT Level-3 KaRIn Low Rate SSH Expert [Data Set], https://doi.org/10.24400/527896/A01-2023.018, 2025b.

Baines, P. G.: Topographic Effects in Stratified Flows, Cambridge Monographs on Mechanics, Cambridge University Press, Cambridge, 2 edn., ISBN 978-1-108-48152-6, https://doi.org/10.1017/9781108673983, 2022.

Barceló-Llull, B., Mason, E., Capet, A., and Pascual, A.: Impact of Vertical and Horizontal Advection on Nutrient Distribution in the Southeast Pacific, Ocean Science, 12, 1003–1011, https://doi.org/10.5194/os-12-1003-2016, 2016.

Bell Jr., T. H.: Topographically Generated Internal Waves in the Open Ocean, Journal of Geophysical Research (1896-1977), 80, 320–327, https://doi.org/10.1029/JC080i003p00320, 1975.

Benavides, M., Berthelot, H., Duhamel, S., Raimbault, P., and Bonnet, S.: Dissolved Organic Matter Uptake by *Trichodesmium* in the Southwest Pacific, Scientific Reports, 7, 41 315, https://doi.org/10.1038/srep41315, 2017.

Benavides, M., Bonnet, S., Le Moigne, F. A. C., Armin, G., Inomura, K., Hallstrøm, S., Riemann, L., Berman-Frank, I., Poletti, E., Garel, M., Grosso, O., Leblanc, K., Guigue, C., Tedetti, M., and Dupouy, C.: Sinking *Trichodesmium* Fixes Nitrogen in the Dark Ocean, The ISME Journal, 16, 2398–2405, https://doi.org/10.1038/s41396-022-01289-6, 2022.

Bendinger, A., Cravatte, S., Gourdeau, L., Brodeau, L., Albert, A., Tchilibou, M., Lyard, F., and Vic, C.: Regional Modeling of Internal-Tide Dynamics around New Caledonia – Part 1: Coherent Internal-Tide Characteristics and Sea Surface Height Signature, Ocean Science, 19, 1315–1338, https://doi.org/10.5194/os-19-1315-2023, 2023.

Bendinger, A., Cravatte, S., Gourdeau, L., Vic, C., and Lyard, F.: Regional Modeling of Internal-Tide Dynamics around New Caledonia – Part 2: Tidal Incoherence and Implications for Sea Surface Height Observability, Ocean Science, 21, 1943–1966, https://doi.org/10.5194/os-21-1943-2025, 2025.

Benzi, R., Ciliberto, S., Baudet, C., Chavarria, G. R., and Tripiccione, R.: Extended Self-Similarity in the Dissipation Range of Fully Developed Turbulence, Europhysics Letters, 24, 275, https://doi.org/10.1209/0295-5075/24/4/007, 1993.

Berthelot, H., Bonnet, S., Grosso, O., Cornet, V., and Barani, A.: Transfer of Diazotroph-Derived Nitrogen towards Non-Diazotrophic Planktonic Communities: A Comparative Study between *Trichodesmium Erythraeum*, *Crocosphaera Watsonii* and *Cyanothece* Sp., Biogeosciences, 13, 4005–4021, https://doi.org/10.5194/bg-13-4005-2016, 2016.

Bonnet, S.: HOPE [Data Set], https://doi.org/10.18142/330, 2024.

Bonnet, S.: HOPE 2025 Cruise, Antea R/V [Data Set], https://doi.org/10.17600/18003527, 2025.

https://doi.org/10.5194/egusphere-2026-3095
Preprint. Discussion started: 12 June 2026


Bonnet, S., Berthelot, H., Turk-Kubo, K., Fawcett, S., Rahav, E., L'Helguen, S., and Berman-Frank, I.: Dynamics of $N_2$ Fixation and Fate of Diazotroph-Derived Nitrogen in a Low-Nutrient, Low-Chlorophyll Ecosystem: Results from the VAHINE Mesocosm Experiment (New Caledonia), Biogeosciences, 13, 2653–2673, https://doi.org/10.5194/bg-13-2653-2016, 2016.

Bonnet, S., Caffin, M., Berthelot, H., and Moutin, T.: Hot Spot of $N_2$ Fixation in the Western Tropical South Pacific Pleads for a Spatial Decoupling between $N_2$ Fixation and Denitrification, Proceedings of the National Academy of Sciences, 114, E2800–E2801, https://doi.org/10.1073/pnas.1619514114, 2017.

Bonnet, S., Berthelot, H., and Berman-Frank, I.: Impact of Diazotrophs on Marine Food Webs and the Biological Carbon Pump: Progress and Remaining Challenges, The ISME Journal, 20, wraf291, https://doi.org/10.1093/ismejo/wraf291, 2026.

Burd, A. B.: Modeling the Vertical Flux of Organic Carbon in the Global Ocean, Annual Review of Marine Science, 16, 135–161, https://doi.org/10.1146/annurev-marine-022123-102516, 2024.

Calil, P. H. R. and Richards, K. J.: Transient Upwelling Hot Spots in the Oligotrophic North Pacific, Journal of Geophysical Research: Oceans, 115, https://doi.org/10.1029/2009JC005360, 2010.

Carli, E., Siegelman, L., Morrow, R., and Vergara, O.: Surface Quasi Geostrophic Reconstruction of Vertical Velocities and Vertical Heat Fluxes in the Southern Ocean: Perspectives for SWOT, Journal of Geophysical Research: Oceans, 129, e2024JC021 216, https://doi.org/10.1029/2024JC021216, 2024.

Charney, J. G.: Geostrophic Turbulence, Journal of the Atmospheric Sciences, 28, 1087–1095, https://doi.org/10.1175/1520-0469(1971)028<1087:GT>2.0.CO;2, 1971.

Chen, W., Jacob, B., Valle-Levinson, A., Stanev, E., Staneva, J., and Badewien, T. H.: Subtidal Secondary Circulation Induced by Eddy Viscosity-Velocity Shear Covariance in a Predominantly Well-Mixed Tidal Inlet, Frontiers in Marine Science, 10, https://doi.org/10.3389/fmars.2023.1105626, 2023.

Chen, X., Wu, Z., and Huang, N. E.: The Time-Dependent Intrinsic Correlation Based on the Empirical Mode Decomposition, Advances in Adaptive Data Analysis, 02, 233–265, https://doi.org/10.1142/S1793536910000471, 2010.

Clements, D. J., Stamieszkin, K., Bianchi, D., Blanco-Bercial, L., Record, N. R., Rodriguez-Perez, R. B., and Maas, A. E.: Active Carbon Transport by Diel Vertical Migrating Zooplankton: Calculated and Modeled, but Never Measured, Annual Review of Marine Science, 18, 301–326, https://doi.org/10.1146/annurev-marine-121422-015330, 2026.

Cohen, J. H. and Forward Jr., R. B.: Zooplankton Diel Vertical Migration — A Review of Proximate Control, in: Oceanography and Marine Biology: An Annual Review, vol. 47, p. 360, CRC Press, Boca Raton, ISBN 978-0-429-13982-6, https://doi.org/10.1201/9781420094220, 2009.

Comby, C., Barrillon, S., Fuda, J.-L., Doglioli, A. M., Tzortzis, R., Grégori, G., Thyssen, M., and Petrenko, A. A.: Measuring Vertical Velocities with ADCPs in Low-Energy Ocean, Journal of Atmospheric and Oceanic Technology, 39, 1669–1684, https://doi.org/10.1175/JTECH-D-21-0180.1, 2022.

Cravatte, S., Kestenare, E., Eldin, G., Ganachaud, A., Lefèvre, J., Marin, F., Menkes, C., and Aucan, J.: Regional Circulation around New Caledonia from Two Decades of Observations, Journal of Marine Systems, 148, 249–271, https://doi.org/10.1016/j.jmarsys.2015.03.004, 2015.

Cushman-Roisin, B.: Introduction to Geophysical Fluid Dynamics, Pearson College Div, Englewood Cliffs, N.J, ISBN 978-0-13-353301-9, 1994.

Dall'Olmo, G., Dingle, J., Polimene, L., Brewin, R. J. W., and Claustre, H.: Substantial Energy Input to the Mesopelagic Ecosystem from the Seasonal Mixed-Layer Pump, Nature Geoscience, 9, 820–823, https://doi.org/10.1038/ngeo2818, 2016.

https://doi.org/10.5194/egusphere-2026-3095
Preprint. Discussion started: 12 June 2026


D'Asaro, E. A.: Turbulent Vertical Kinetic Energy in the Ocean Mixed Layer, Journal of Physical Oceanography, 31, 3530–3537, https://doi.org/10.1175/1520-0485(2002)031<3530:TVKEIT>2.0.CO;2, 2001.

D'Asaro, E. A.: Turbulence in the Upper-Ocean Mixed Layer, Annual Review of Marine Science, 6, 101–115, https://doi.org/10.1146/annurev-marine-010213-135138, 2014.

D'Asaro, E. A., Farmer, D. M., Osse, J. T., and Dairiki, G. T.: A Lagrangian Float, Journal of Atmospheric and Oceanic Technology, 13, 1230–1246, https://doi.org/10.1175/1520-0426(1996)013<1230:ALF>2.0.CO;2, 1996.

D'Asaro, E. A., Lien, R.-C., and Henyey, F.: High-Frequency Internal Waves on the Oregon Continental Shelf, Journal of Physical Oceanography, 37, 1956–1967, https://doi.org/10.1175/JPO3096.1, 2007.

D'Asaro, E. A., Shcherbina, A. Y., Klymak, J. M., Molemaker, J., Novelli, G., Guigand, C. M., Haza, A. C., Haus, B. K., Ryan, E. H., Jacobs, G. A., Huntley, H. S., Laxague, N. J. M., Chen, S., Judt, F., McWilliams, J. C., Barkan, R., Kirwan, A. D., Poje, A. C., and Özgökmen, T. M.: Ocean Convergence and the Dispersion of Flotsam, Proceedings of the National Academy of Sciences, 115, 1162–1167, https://doi.org/10.1073/pnas.1718453115, 2018.

Denman, K. L. and Gargett, A. E.: Time and Space Scales of Vertical Mixing and Advection of Phytoplankton in the Upper Ocean, Limnology and Oceanography, 28, 801–815, https://doi.org/10.4319/lo.1983.28.5.0801, 1983.

Derot, J., Schmitt, F. G., Gentilhomme, V., and Morin, P.: Correlation between Long-Term Marine Temperature Time Series from the Eastern and Western English Channel: Scaling Analysis Using Empirical Mode Decomposition, Comptes Rendus Geoscience, 348, 343–349, https://doi.org/10.1016/j.crte.2015.12.001, 2016.

Ferrari, R. and Wunsch, C.: Ocean Circulation Kinetic Energy: Reservoirs, Sources, and Sinks, Annual Review of Fluid Mechanics, 41, 253–282, https://doi.org/10.1146/annurev.fluid.40.111406.102139, 2009.

Flagg, C. N. and Smith, S. L.: On the Use of the Acoustic Doppler Current Profiler to Measure Zooplankton Abundance, Deep Sea Research Part A. Oceanographic Research Papers, 36, 455–474, https://doi.org/10.1016/0198-0149(89)90047-2, 1989.

Flandrin, P. and Gonçalvès, P.: Empirical Mode Decompositions as Data-Driven Wavelet-like Expansions, International Journal of Wavelets, Multiresolution and Information Processing, 02, 477–496, https://doi.org/10.1142/S0219691304000561, 2004.

Flandrin, P., Rilling, G., and Goncalves, P.: Empirical Mode Decomposition as a Filter Bank, IEEE Signal Processing Letters, 11, 112–114, https://doi.org/10.1109/LSP.2003.821662, 2004.

Forward, R. B.: Light and Diurnal Vertical Migration: Photobehavior and Photophysiology of Plankton, in: Photochemical and Photobiological Reviews: Volume 1, edited by Smith, K. C., pp. 157–209, Springer US, Boston, MA, ISBN 978-1-4684-2574-1, https://doi.org/10.1007/978-1-4684-2574-1_4, 1976.

Freilich, M. A. and Mahadevan, A.: Decomposition of Vertical Velocity for Nutrient Transport in the Upper Ocean, Journal of Physical Oceanography, 49, 1561–1575, https://doi.org/10.1175/JPO-D-19-0002.1, 2019.

Fuchs, R., Rossi, V., Caille, C., Bensoussan, N., Pinazo, C., Grosso, O., and Thyssen, M.: Intermittent Upwelling Events Trigger Delayed, Major, and Reproducible Pico-Nanophytoplankton Responses in Coastal Oligotrophic Waters, Geophysical Research Letters, 50, e2022GL102 651, https://doi.org/10.1029/2022GL102651, 2023.

Ganachaud, A., Vega, A., Rodier, M., Dupouy, C., Maes, C., Marchesiello, P., Eldin, G., Ridgway, K., and Le Borgne, R.: Observed Impact of Upwelling Events on Water Properties and Biological Activity off the Southwest Coast of New Caledonia, Marine Pollution Bulletin, 61, 449–464, https://doi.org/10.1016/j.marpolbul.2010.06.042, 2010.

Gao, Y., Schmitt, F. G., Hu, J., and Huang, Y.: Scaling Analysis of the CFOSAT Along Track Wind and Wave Data [Code], GitHub, https://github.com/lanlankai/Scaling-Analysis-of-the-CFOSAT-Along-Track-Wind-and-Wave-Data, 2021a.

https://doi.org/10.5194/egusphere-2026-3095
Preprint. Discussion started: 12 June 2026


Gao, Y., Schmitt, F. G., Hu, J., and Huang, Y.: Scaling Analysis of the China France Oceanography Satellite Along-Track Wind and Wave Data, Journal of Geophysical Research: Oceans, 126, e2020JC017 119, https://doi.org/10.1029/2020JC017119, 2021b.

Garrett, C.: Mixing in the Ocean Interior, Dynamics of Atmospheres and Oceans, 3, 239–265, https://doi.org/10.1016/0377-0265(79)90011-3, 1979.

Garrett, C. and Munk, W.: Internal Waves in the Ocean, Annual Review of Fluid Mechanics, 11, 339–369, https://doi.org/10.1146/annurev.fl.11.010179.002011, 1979.

Gordon, R. L. and Marshall, N. F.: Submarine Canyons: Internal Wave Traps?, Geophysical Research Letters, 3, 622–624, https://doi.org/10.1029/GL003i010p00622, 1976.

Hanson, C. E., Pattiaratchi, C. B., and Waite, A. M.: Sporadic Upwelling on a Downwelling Coast: Phytoplankton Responses to Spatially Variable Nutrient Dynamics off the Gascoyne Region of Western Australia, Continental Shelf Research, 25, 1561–1582, https://doi.org/10.1016/j.csr.2005.04.003, 2005.

Hays, G. C.: A Review of the Adaptive Significance and Ecosystem Consequences of Zooplankton Diel Vertical Migrations, Hydrobiologia, 503, 163–170, https://doi.org/10.1023/B:HYDR.0000008476.23617.b0, 2003.

He, J. and Mahadevan, A.: Vertical Velocity Diagnosed From Surface Data With Machine Learning, Geophysical Research Letters, 51, e2023GL104 835, https://doi.org/10.1029/2023GL104835, 2024.

Helske, J. and Luukko, P.: Rlibeemd: Ensemble Empirical Mode Decomposition (EEMD) and Its Complete Variant (CEEMDAN), Version 1.4.4 [Code], CRAN, https://doi.org/10.32614/CRAN.package.Rlibeemd, 2025.

Hersbach, H., Bell, B., Berrisford, P., Hirahara, S., Horányi, A., Muñoz-Sabater, J., Nicolas, J., Peubey, C., Radu, R., Schepers, D., Simmons, A., Soci, C., Abdalla, S., Abellan, X., Balsamo, G., Bechtold, P., Biavati, G., Bidlot, J., Bonavita, M., De Chiara, G., Dahlgren, P., Dee, D., Diamantakis, M., Dragani, R., Flemming, J., Forbes, R., Fuentes, M., Geer, A., Haimberger, L., Healy, S., Hogan, R. J., Hólm, E., Janisková, M., Keeley, S., Laloyaux, P., Lopez, P., Lupu, C., Radnoti, G., de Rosnay, P., Rozum, I., Vamborg, F., Villaume, S., and Thépaut, J.-N.: The ERA5 Global Reanalysis, Quarterly Journal of the Royal Meteorological Society, 146, 1999–2049, https://doi.org/10.1002/qj.3803, 2020.

Houpert, L., Durrieu de Madron, X., Testor, P., Bosse, A., D'Ortenzio, F., Bouin, M. N., Dausse, D., Le Goff, H., Kunesch, S., Labaste, M., Coppola, L., Mortier, L., and Raimbault, P.: Observations of Open-Ocean Deep Convection in the Northwestern Mediterranean Sea: Seasonal and Interannual Variability of Mixing and Deep Water Masses for the 2007-2013 Period, Journal of Geophysical Research: Oceans, 121, 8139–8171, https://doi.org/10.1002/2016JC011857, 2016.

Huang, N. E., Shen, Z., Long, S. R., Wu, M. C., Shih, H. H., Zheng, Q., Yen, N.-C., Tung, C. C., and Liu, H. H.: The Empirical Mode Decomposition and the Hilbert Spectrum for Nonlinear and Non-Stationary Time Series Analysis, Proceedings of the Royal Society of London. Series A: Mathematical, Physical and Engineering Sciences, 454, 903–995, https://doi.org/10.1098/rspa.1998.0193, 1998.

Huang, Y. and Schmitt, F. G.: Time Dependent Intrinsic Correlation Analysis of Temperature and Dissolved Oxygen Time Series Using Empirical Mode Decomposition, Journal of Marine Systems, 130, 90–100, https://doi.org/10.1016/j.jmarsys.2013.06.007, 2014.

Huang, Y., Schmitt, F. G., Lu, Zhiming., and Liu, Y.: Analysis of Daily River Flow Fluctuations Using Empirical Mode Decomposition and Arbitrary Order Hilbert Spectral Analysis, Journal of Hydrology, 373, 103–111, https://doi.org/10.1016/j.jhydrol.2009.04.015, 2009.

Huang, Y. X., Schmitt, F. G., Lu, Z. M., and Liu, Y. L.: An Amplitude-Frequency Study of Turbulent Scaling Intermittency Using Empirical Mode Decomposition and Hilbert Spectral Analysis, Europhysics Letters, 84, 40 010, https://doi.org/10.1209/0295-5075/84/40010, 2008.

Kämpf, J.: Wind-Driven Overturning, Mixing and Upwelling in Shallow Water: A Nonhydrostatic Modeling Study, Journal of Marine Science and Engineering, 5, 47, https://doi.org/10.3390/jmse5040047, 2017.

https://doi.org/10.5194/egusphere-2026-3095
Preprint. Discussion started: 12 June 2026


Kämpf, J. and Chapman, P.: Upwelling Systems of the World, Springer International Publishing, Cham, ISBN 978-3-319-42522-1 978-3-319-42524-5, https://doi.org/10.1007/978-3-319-42524-5, 2016.

Katul, G. and Chu, C.-R.: A Theoretical and Experimental Investigation of Energy-Containing Scales in the Dynamic Sublayer of Boundary-Layer Flows, Boundary-Layer Meteorology, 86, 279–312, https://doi.org/10.1023/A:1000657014845, 1998.

Katul, G. G., Porporato, A., and Nikora, V.: Existence of $K^{-1}$ Power-Law Scaling in the Equilibrium Regions of Wall-Bounded Turbulence Explained by Heisenberg's Eddy Viscosity, Physical Review E, 86, 066 311, https://doi.org/10.1103/PhysRevE.86.066311, 2012.

Kbaier Ben Ismail, D., Lazure, P., and Puillat, I.: Advanced Spectral Analysis and Cross Correlation Based on the Empirical Mode Decomposition: Application to the Environmental Time Series, IEEE Geoscience and Remote Sensing Letters, 12, 1968–1972, https://doi.org/10.1109/LGRS.2015.2441374, 2015.

Kelley, D., Richards, C., and WG127 SCOR/IAPSO: Gsw: Gibbs Sea Water Functions, Version 1.2-0 [Code], CRAN, https://doi.org/10.32614/CRAN.package.gsw, 2024.

Khintchine, A.: Korrelationstheorie der stationären stochastischen Prozesse, Mathematische Annalen, 109, 604–615, https://doi.org/10.1007/BF01449156, 1934.

Klinck, J. M.: Circulation near Submarine Canyons: A Modeling Study, Journal of Geophysical Research: Oceans, 101, 1211–1223, https://doi.org/10.1029/95JC02901, 1996.

Klymak, J. M. and Moum, J. N.: Oceanic Isopycnal Slope Spectra. Part I: Internal Waves, Journal of Physical Oceanography, 37, 1215–1231, https://doi.org/10.1175/JPO3073.1, 2007a.

Klymak, J. M. and Moum, J. N.: Oceanic Isopycnal Slope Spectra. Part II: Turbulence, Journal of Physical Oceanography, 37, 1232–1245, https://doi.org/10.1175/JPO3074.1, 2007b.

Kolmogorov, A. N.: On Degeneration (Decay) of Isotropic Turbulence in an Incompressible Viscous Liquid, in: Doklady Akademii Nauk SSSR, vol. 31, pp. 538–540, 1941.

Kolmogorov, A. N.: A Refinement of Previous Hypotheses Concerning the Local Structure of Turbulence in a Viscous Incompressible Fluid at High Reynolds Number, Journal of Fluid Mechanics, 13, 82–85, https://doi.org/10.1017/S0022112062000518, 1962.

Landou, E., Lazar, B., LaRoche, J., Fennel, K., and Berman-Frank, I.: Contribution of Photic and Aphotic $N_2$ Fixation to Production in an Oligotrophic Sea, Limnology and Oceanography, 68, 692–708, https://doi.org/10.1002/lno.12303, 2023.

Lewis, M. R., Hebert, D., Harrison, W. G., Platt, T., and Oakey, N. S.: Vertical Nitrate Fluxes in the Oligotrophic Ocean, Science, 234, 870–873, https://doi.org/10.1126/science.234.4778.870, 1986.

Liang, X., Spall, M., and Wunsch, C.: Global Ocean Vertical Velocity From a Dynamically Consistent Ocean State Estimate, Journal of Geophysical Research: Oceans, 122, 8208–8224, https://doi.org/10.1002/2017JC012985, 2017.

Lilover, M.-J., Laanemets, J., Kullas, T., Stips, A., and Kononen, K.: Late summer vertical nutrient fluxes estimated from direct turbulence measurements: a Gulf of Finland case study., Proceedings of the Estonian Academy of Sciences, Biology, Ecology, 52, 193, https://openurl.ebsco.com/contentitem/gcd:10953781?sid=ebsco:plink:crawler&id=ebsco:gcd:10953781, 2003.

Lovejoy, S. and Schertzer, D.: Haar Wavelets, Fluctuations and Structure Functions: Convenient Choices for Geophysics, Nonlinear Processes in Geophysics, 19, 513–527, https://doi.org/10.5194/npg-19-513-2012, 2012.

Lovejoy, S. and Schertzer, D.: The Weather and Climate: Emergent Laws and Multifractal Cascades, Cambridge University Press, ISBN 978-1-107-01898-3, 2013.

https://doi.org/10.5194/egusphere-2026-3095
Preprint. Discussion started: 12 June 2026


Ma, L., Bai, X., Laws, E. A., Xiao, W., Guo, C., Liu, X., Chiang, K.-P., Gao, K., and Huang, B.: Responses of Phytoplankton Communities to Internal Waves in Oligotrophic Oceans, Journal of Geophysical Research: Oceans, 128, e2023JC020 201, https://doi.org/10.1029/2023JC020201, 2023.

Marchesiello, P., Lefèvre, J., Vega, A., Couvelard, X., and Menkes, C.: Coastal Upwelling, Circulation and Heat Balance around New Caledonia's Barrier Reef, Marine Pollution Bulletin, 61, 432–448, https://doi.org/10.1016/j.marpolbul.2010.06.043, 2010.

McDougall, T. J.: Thermodynamic Concepts Used in Physical Oceanography, Ocean Science, 22, 923–960, https://doi.org/10.5194/os-22-923-2026, 2026.

Nowicki, M., DeVries, T., and Siegel, D. A.: Quantifying the Carbon Export and Sequestration Pathways of the Ocean's Biological Carbon Pump, Global Biogeochemical Cycles, 36, e2021GB007 083, https://doi.org/10.1029/2021GB007083, 2022.

Obukhov, A. M.: On the Distribution of Energy in the Spectrum of Turbulent Flow, Doklady Akademii Nauk SSSR, 32, 22, https://cir.nii.ac.jp/crid/1371131420873447168, 1941.

Ott, M. W.: The Accuracy of Acoustic Vertical Velocity Measurements: Instrument Biases and the Effect of Zooplankton Migration, Continental Shelf Research, 25, 243–257, https://doi.org/10.1016/j.csr.2004.09.007, 2005.

Pan, X., Wong, G. T. F., Shiah, F.-K., and Ho, T.-Y.: Enhancement of Biological Productivity by Internal Waves: Observations in the Summertime in the Northern South China Sea, Journal of Oceanography, 68, 427–437, https://doi.org/10.1007/s10872-012-0107-y, 2012.

Parseval des Chênes, M.-A.: Mémoire Sur Les Séries et Sur l'intégration Complète d'une Équation Aux Différences Partielles Linéaires Du Second Ordre, à Coefficients Constants, Mémoires présentés à l'Institut des Sciences, Lettres et Arts, par divers savants, et lus dans ses assemblées. Sciences, mathématiques et physiques. (Savants étrangers), 1, 42, first presented to the Academy of Sciences (Paris) on April 5, 1799, 1806.

Petrenko, A. A., Robache, K., and Gentil, M.: High-Frequency Time Series of Vertical and Horizontal Velocity Components Measured Offshore New-Caledonia between March 2024 and February 2025, https://doi.org/10.17882/114360, 2026.

Petruncio, E. T., Rosenfeld, L. K., and Paduan, J. D.: Observations of the Internal Tide in Monterey Canyon, Journal of Physical Oceanography, 28, 1873–1903, https://doi.org/10.1175/1520-0485(1998)028<1873:OOTITI>2.0.CO;2, 1998.

Plancherel, M.: Contribution à l'étude de la représentation d'une fonction arbitraire par des intégrales définies, Rendiconti del Circolo Matematico di Palermo (1884-1940), 30, 289–335, https://doi.org/10.1007/BF03014877, 1910.

Polzin, K. L. and Lvov, Y. V.: Toward Regional Characterizations of the Oceanic Internal Wavefield, Reviews of Geophysics, 49, https://doi.org/10.1029/2010RG000329, 2011.

Relvas, P. and Barton, E. D.: A Separated Jet and Coastal Counterflow during Upwelling Relaxation off Cape São Vicente (Iberian Peninsula), Continental Shelf Research, 25, 29–49, https://doi.org/10.1016/j.csr.2004.09.006, 2005.

Renosh, P. R., Schmitt, F. G., Loisel, H., Sentchev, A., and Mériaux, X.: High Frequency Variability of Particle Size Distribution and Its Dependency on Turbulence over the Sea Bottom during Re-Suspension Processes, Continental Shelf Research, 77, 51–60, https://doi.org/10.1016/j.csr.2014.01.024, 2014.

Renosh, P. R., Schmitt, F. G., and Loisel, H.: Intermittent Particle Dynamics in Marine Coastal Waters, Nonlinear Processes in Geophysics, 22, 633–643, https://doi.org/10.5194/npg-22-633-2015, 2015.

Richardson, L. F.: Weather Prediction by Numerical Process, Cambridge, The University press, http://archive.org/details/weatherpredictio00richrich, 1922.

https://doi.org/10.5194/egusphere-2026-3095
Preprint. Discussion started: 12 June 2026


Robache, K. and Schmitt, F. G.: Multiscale Statistical Analysis of Thermal and Non-Thermal Components of Seawater $pCO_2$ in the Western English Channel: Scaling, Time-Reversibility, and Dependence, Biogeosciences, 22, 8093–8111, https://doi.org/10.5194/bg-22-8093-2025, 2025a.

Robache, K. and Schmitt, F. G.: PDF Quotient Code [Code], GitHub and Zenodo, https://doi.org/10.5281/zenodo.18420016, 2025b.

Robache, K. and Schmitt, F. G.: Lagrangian Scaling and Intermittency of Turbulent CARbon Interface OCean Atmosphere (CARIOCA) Time Series in the Southern Ocean, Journal of Geophysical Research: Oceans, 131, e2025JC023 080, https://doi.org/10.1029/2025JC023080, 2026a.

Robache, K. and Schmitt, F. G.: Dynamics and Extremes of Open Ocean Non-thermal $pCO_2$ Time Series, Authorea, ESS Open Archive, pp. 1–15, https://doi.org/10.22541/essoar.177038994.43181623/v1, 2026b.

Robache, K., Schmitt, F. G., and Huang, Y.: Scaling and Intermittent Properties of Oceanic and Atmospheric $pCO_2$ Time Series and Their Difference in a Turbulence Framework, Nonlinear Processes in Geophysics, 32, 35–49, https://doi.org/10.5194/npg-32-35-2025, 2025.

Rodríguez, J., Tintoré, J., Allen, J. T., Blanco, J. M., Gomis, D., Reul, A., Ruiz, J., Rodríguez, V., Echevarría, F., and Jiménez-Gómez, F.: Mesoscale Vertical Motion and the Size Structure of Phytoplankton in the Ocean, Nature, 410, 360–363, https://doi.org/10.1038/35066560, 2001.

Rousselet, L., Doglioli, A. M., de Verneil, A., Pietri, A., Della Penna, A., Berline, L., Marrec, P., Grégori, G., Thyssen, M., Carlotti, F., Barrillon, S., Simon-Bot, F., Bonal, M., d'Ovidio, F., and Petrenko, A.: Vertical Motions and Their Effects on a Biogeochemical Tracer in a Cyclonic Structure Finely Observed in the Ligurian Sea, Journal of Geophysical Research: Oceans, 124, 3561–3574, https://doi.org/10.1029/2018JC014392, 2019.

Rousselet, L., d'Ovidio, F., Izard, L., Penna, A. D., Petrenko, A., Barrillon, S., Nencioli, F., and Doglioli, A.: A Software Package for an Adaptive Satellite-Based Sampling for Oceanographic Cruises (SPASSOv2.0): Tracking Fine-Scale Features for Physical and Biogeochemical Studies, Journal of Atmospheric and Oceanic Technology, 42, 979–990, https://doi.org/10.1175/JTECH-D-24-0071.1, 2025.

Savarino, M., Moigne, F. A. C. L., Jardin-Camps, M., Ababou, F.-E., Grosso, O., de Saint-Léger, E., Leridant, A., Laurenceau-Cornec, E. C., Bachelier, C., Vignon, D., and Bonnet, S.: Comparable Carbon Export Fluxes but Divergent Pathways across Contrasting $N_2$ Fixation Regimes, Authorea, pp. 1–80, https://doi.org/10.22541/au.176650665.54437898/v1, 2025.

Schmitt, F. G.: Linking Eulerian and Lagrangian Structure Functions' Scaling Exponents in Turbulence, Physica A: Statistical Mechanics and its Applications, 368, 377–386, https://doi.org/10.1016/j.physa.2005.12.028, 2006.

Schmitt, F. G. and Huang, Y.: Stochastic Analysis of Scaling Time Series: From Turbulence Theory to Applications, Cambridge University Press, ISBN 978-1-107-06761-5, 2016.

Schott, F. and Johns, W.: Half-Year-Long Measurements with a Buoy-Mounted Acoustic Doppler Current Profiler in the Somali Current, Journal of Geophysical Research: Oceans, 92, 5169–5176, https://doi.org/10.1029/JC092iC05p05169, 1987.

Shao, Z., Xu, Y., Wang, H., Luo, W., Wang, L., Huang, Y., Agawin, N. S. R., Ahmed, A., Benavides, M., Bentzon-Tilia, M., Berman-Frank, I., Berthelot, H., Biegala, I. C., Bif, M. B., Bode, A., Bonnet, S., Bronk, D. A., Brown, M. V., Campbell, L., Capone, D. G., Carpenter, E. J., Cassar, N., Chang, B. X., Chappell, D., Chen, Y.-l. L., Church, M. J., Cornejo-Castillo, F. M., Detoni, A. M. S., Doney, S. C., Dupouy, C., Estrada, M., Fernandez, C., Fernández-Castro, B., Fonseca-Batista, D., Foster, R. A., Furuya, K., Garcia, N., Goto, K., Gago, J., Gradoville, M. R., Hamersley, M. R., Henke, B. A., Hörstmann, C., Jayakumar, A., Jiang, Z., Kao, S.-J., Karl, D. M., Kittu, L. R., Knapp, A. N., Kumar, S., LaRoche, J., Liu, H., Liu, J., Lory, C., Löscher, C. R., Marañón, E., Messer, L. F., Mills, M. M., Mohr, W., Moisander, P. H., Mahaffey, C., Moore, R., Mouriño-Carballido, B., Mulholland, M. R., Nakaoka, S.-i., Needoba, J. A., Raes, E. J., Rahav, E., Ramírez-Cárdenas, T., Reeder, C. F., Riemann, L., Riou, V., Robidart, J. C., Sarma, V. V. S. S., Sato, T., Saxena, H., Selden, C., Seymour, J. R., Shi, D., Shiozaki,

https://doi.org/10.5194/egusphere-2026-3095
Preprint. Discussion started: 12 June 2026


T., Singh, A., Sipler, R. E., Sun, J., Suzuki, K., Takahashi, K., Tan, Y., Tang, W., Tremblay, J.-É., Turk-Kubo, K., Wen, Z., White, A. E., Wilson, S. T., Yoshida, T., Zehr, J. P., Zhang, R., Zhang, Y., and Luo, Y.-W.: Global Oceanic Diazotroph Database Version 2 and Elevated Estimate of Global Oceanic $N_2$ Fixation, Earth System Science Data, 15, 3673–3709, https://doi.org/10.5194/essd-15-3673-2023, 2023.

SHOM-IRD: Bathymetric Digital Elevation Model of the New Caledonia Seafront (TSUCAL Project) [Data Set], https://doi.org/10.17183/MNT_NC100m_TSUCAL_WGS84, 2021.

Siegel, D. A., DeVries, T., Cetinić, I., and Bisson, K. M.: Quantifying the Ocean's Biological Pump and Its Carbon Cycle Impacts on Global Scales, Annual Review of Marine Science, 15, 329–356, https://doi.org/10.1146/annurev-marine-040722-115226, 2023.

Skyllingstad, E. D., Paluszkiewicz, T., Denbo, D. W., and Smyth, W. D.: Nonlinear Vertical Mixing Processes in the Ocean: Modeling and Parameterization, Physica D: Nonlinear Phenomena, 98, 574–593, https://doi.org/10.1016/0167-2789(96)00113-3, 1996.

Song, Y. T. and Chao, Y.: A Theoretical Study of Topographic Effects on Coastal Upwelling and Cross-Shore Exchange, Ocean Modelling, 6, 151–176, https://doi.org/10.1016/S1463-5003(02)00064-1, 2004.

Spurgin, J. M. and Allen, S. E.: Flow Dynamics around Downwelling Submarine Canyons, Ocean Science, 10, 799–819, https://doi.org/10.5194/os-10-799-2014, 2014.

Stammer, D.: Global Characteristics of Ocean Variability Estimated from Regional TOPEX/POSEIDON Altimeter Measurements, Journal of Physical Oceanography, 27, 1743–1769, https://doi.org/10.1175/1520-0485(1997)027<1743:GCOOVE>2.0.CO;2, 1997.

Strass, V. H.: Chlorophyll Patchiness Caused by Mesoscale Upwelling at Fronts, Deep Sea Research Part A. Oceanographic Research Papers, 39, 75–96, https://doi.org/10.1016/0198-0149(92)90021-K, 1992.

Taylor, J. R. and Thompson, A. F.: Submesoscale Dynamics in the Upper Ocean, Annual Review of Fluid Mechanics, 55, 103–127, https://doi.org/10.1146/annurev-fluid-031422-095147, 2023.

Thurnherr, A. M.: Vertical Velocity from LADCP Data, in: 2011 IEEE/OES 10th Current, Waves and Turbulence Measurements (CWTM), pp. 198–204, IEEE, Monterey, CA, USA, ISBN 978-1-4244-9285-5, https://doi.org/10.1109/CWTM.2011.5759552, 2011.

Thurnherr, A. M., Kunze, E., Toole, J. M., St. Laurent, L., Richards, K. J., and Ruiz-Angulo, A.: Vertical Kinetic Energy and Turbulent Dissipation in the Ocean, Geophysical Research Letters, 42, 7639–7647, https://doi.org/10.1002/2015GL065043, 2015.

Tzortzis, R., Doglioli, A. M., Barrillon, S., Petrenko, A. A., d'Ovidio, F., Izard, L., Thyssen, M., Pascual, A., Barceló-Llull, B., Cyr, F., Tedetti, M., Bhairy, N., Garreau, P., Dumas, F., and Gregori, G.: Impact of Moderately Energetic Fine-Scale Dynamics on the Phytoplankton Community Structure in the Western Mediterranean Sea, Biogeosciences, 18, 6455–6477, https://doi.org/10.5194/bg-18-6455-2021, 2021.

van Haren, H.: Monthly Periodicity in Acoustic Reflections and Vertical Motions in the Deep Ocean, Geophysical Research Letters, 34, https://doi.org/10.1029/2007GL029947, 2007.

van Haren, H.: Self-Regulation of Deep-Ocean Internal Wave Continuum: Observations on Related near-Inertial Shear and High-Frequency Vertical Motions, Geophysical Research Letters, 35, https://doi.org/10.1029/2007GL032697, 2008.

van Haren, H.: A Composite Vertical Current Spectrum for Strongly and Weakly Stratified Seas and Oceans, Journal of Marine Research, 73, https://elischolar.library.yale.edu/journal_of_marine_research/403, 2015.

van Haren, H. and Compton, T. J.: Diel Vertical Migration in Deep Sea Plankton Is Finely Tuned to Latitudinal and Seasonal Day Length, PLoS ONE, 8, e64 435, https://doi.org/10.1371/journal.pone.0064435, 2013.

Wickham, H. and RStudio: Tidyverse: Easily Install and Load the "Tidyverse", Version 2.0.0 [Code], CRAN, https://doi.org/10.32614/CRAN.package.tidyverse, 2023.

Wiener, N.: Generalized Harmonic Analysis, Acta Mathematica, 55, 117–258, https://doi.org/10.1007/BF02546511, 1930.

https://doi.org/10.5194/egusphere-2026-3095
Preprint. Discussion started: 12 June 2026


Wu, Z. and Huang, N. E.: Ensemble Empirical Mode Decomposition: A Noise-Assisted Data Analysis Method, Advances in Adaptive Data Analysis, 01, 1–41, https://doi.org/10.1142/S1793536909000047, 2009.

Wunsch, C. and Ferrari, R.: Vertical Mixing, Energy, and the General Circulation of the Oceans, Annual Review of Fluid Mechanics, 36, 281–314, https://doi.org/10.1146/annurev.fluid.36.050802.122121, 2004.

Xu, H., Ouellette, N. T., and Bodenschatz, E.: Curvature of Lagrangian Trajectories in Turbulence, Physical Review Letters, 98, 050 201, https://doi.org/10.1103/PhysRevLett.98.050201, 2007.

Zhu, R., Li, Y., Chen, Z., Du, T., Zhang, Y., Li, Z., Jing, Z., Yang, H., Jing, Z., and Wu, L.: Deep Learning Improves Reconstruction of Ocean Vertical Velocity, Geophysical Research Letters, 50, e2023GL104 889, https://doi.org/10.1029/2023GL104889, 2023.